MNRAS 000, 1–16 (2026) Preprint 9 September 2026 Compiled using MNRAS LaTeX style file v3.3

V453 Cyg: a tidally perturbed β Cep star in an eclipsing binary with changing pulsation axis and apsidal motion

A. Moharana,[1★] J. Southworth,[1] D. M. Bowman,[2,3] S. Rosu,[4] G. Handler,[5] and F. Marcadon[6]
[1] Astrophysics Group, Keele University, Staffordshire, ST5 5BG, UK
[2] School of Mathematics, Statistics and Physics, Newcastle University, Newcastle upon Tyne, NE1 7RU, UK
[3] Institute of Astronomy, KU Leuven, Celesijnenlaan 200D, 3001 Leuven, Belgium
[4] Department of Astronomy, University of Geneva, Chemin Pegasi 51, 1290 Versoix, Switzerland
[5] Nicolaus Copernicus Astronomical Center, Polish Academy of Sciences, ul. Bartycka 18, PL-00-716 Warszawa, Poland
[6] Private Researcher, Orléans, France

Accepted XXX. Received YYY; in original form ZZZ

ABSTRACT

V453 Cyg is an eclipsing binary in the open cluster NGC 6871 consisting of two B-type stars. It shows β Cep pulsations and has been the focus of many studies investigating the problem of the mass discrepancy in massive stars. We present a comprehensive analysis of V453 Cyg using nine sectors of *TESS* observations and 28 HERMES binary-phase-resolved échelle spectra. We find that the primary has a mass of 14.56±0.13 $M_\odot$ and a radius of 8.575±0.032 $R_\odot$ while the secondary has a mass of 11.103±0.065 $M_\odot$ and a radius of 5.378±0.030 $R_\odot$. We find that several pulsation frequencies vary in their amplitude and phase over time. Moreover, the dominant β Cep pulsation mode in the primary is tidally perturbed, with it being split into at least three frequencies. We analyse the amplitude variations of the dominant mode using the oblique pulsator model and find that the pulsation axis of the primary is changing over the nine *TESS* sectors, and possibly precessing. V453 Cyg also shows apsidal motion at the rate of 4.1±0.4° yr^{-1}, and corresponds to a weighted-average mean of the internal stellar structure constant of $\bar{k}_2 = 0.0046 \pm 0.0005$. Therefore, V453 Cyg presents an interesting case to study the impact of tides on the evolution of close binaries.

Key words: asteroseismology – binaries: eclipsing – stars: fundamental parameters – stars: massive – stars: individual: V453 Cyg

1 INTRODUCTION

A pulsator in a spectroscopic double-lined eclipsing binary (DLEB) allows us to get direct measurements of the mass, radius, effective temperature, and metallicity, along with constraints on the stellar structure (see Southworth & Bowman 2026 for a detailed review). However, the additional companion can alter the pulsations in both interacting (Rui & Fuller 2021; Wagg et al. 2024; Henneco et al. 2025; Miszuda et al. 2025; Henneco & Bowman 2026) and non-interacting cases (Hambleton et al. 2013; Kołaczek-Szymański et al. 2021; Handler et al. 2022).

Most massive stars are pulsators (Bowman 2020) and predominantly exist in multiple systems (Sana et al. 2012; Offner et al. 2023) Therefore, it is expected that most β Cep pulsators exist not only in binary systems (Bowman 2020; Southworth & Bowman 2022; Eze & Handler 2024) but also higher-order multiple systems (e.g. Moharana et al. 2026). The high multiplicity of massive stars results in higher instances of stellar interactions (Sana et al. 2012). These interactions produce detectable changes that have been measured as period changes (Laur et al. 2015), apsidal motion (Rosu et al. 2022a), and even eclipse depth variations (Baum et al. 2025). Consequently, different physical processes in massive binary systems may produce detectable variations in stellar pulsations.

★ E-mail: dr.ayush.moharana@gmail.com, a.moharana@keele.ac.uk

An important physical process that affects binary evolution is the tidal force. The tidal force in stars is exhibited in two distinct forms: dynamical tide and equilibrium tide. Dynamical tides act on the radiative zones in a star, while equilibrium tides act on the convective zones (Zahn 1977; Hut 1981; Savonije & Papaloizou 1984; Zahn & Bouchet 1989; Kushnir et al. 2017; Esseldeurs et al. 2024) Therefore, in massive stars, dynamical tides are dominant. But as massive stars evolve, they develop subsurface convective zones. This causes both dynamical tides and equilibrium tides to be active in massive stars, even in the parts of the main-sequence phase (Sciarini et al. 2026).

Zahn & Bouchet (1989) showed that the dissipation of equilibrium tide results in circularisation of the orbit and synchronisation of the stars' rotation rate with the binary orbit. But recent hydrodynamical simulations suggest that dynamical tide is also needed to get the complete picture (Ogilvie & Lesur 2012; Duguid et al. 2020; Sciarini et al. 2026) with the circularisation being powered through the tidal dissipation by internal gravity waves (Fuller & Lai 2012a,b; Fuller et al. 2017; Barker 2022). Moreover, the dynamical tide can also excite tidally excited oscillations (TEOs; Hambleton et al. 2013; Fuller 2017; Guo 2021) while the equilibrium tide can lead to tidally perturbed pulsations (TPPs; Bowman et al. 2019; Handler et al. 2020, 2022 — see reviews by Guo 2021 and Southworth & Bowman 2026). Therefore, understanding the interplay between stellar tide and pulsations is essential for understanding the evolution of close binary systems.

Changes in stellar pulsations also provide an avenue to understand physical processes in binary systems. It is expected that with stellar evolution, the pulsations in a star will change, but such effects are hard to observe on human timescales (see Bowman 2017). Nonetheless, there have been several instances of observed variation in stellar pulsations. Amplitude variations have been observed in RR Lyr stars[1] (Carrell et al. 2024), δ Sct stars (Breger 2000; Bowman et al. 2016, 2021), white dwarfs (Kepler et al. 2003; Handler & WET network of collaborators 2013), supergiants (Abt et al. 2023), Cepheids (Turner et al. 2005), and roAp stars (Medupe et al. 2015). For example, the roAp star HD 60435 even stopped pulsating within one week and has since been photometrically stable for years (Kurtz et al. 2025). Of particular relevance for this paper, β Cep stars also show amplitude variations. For example, the β Cep binary system Spica had one frequency of 5.75 d^{-1} that decreased in amplitude (Tkachenko et al. 2016), and HD 180642 had several pulsations with amplitude variations (Degroote et al. 2009; Degroote 2013). The most famous example of a β Cep star with amplitude variations is 16 Lac. It was followed extensively using multisite observations and showed amplitude variations of several modes on timescales ranging from a few hundred days to tens of years (Jerzykiewicz et al. 2015).

Amplitude variability of coherently excited pulsation modes has been attributed to various phenomena, including: (i) time-dependent imbalances in driving and damping (Murphy et al. 2012; Bowman et al. 2021; Kurtz et al. 2025), (ii) convection-pulsation interactions (Abt et al. 2023), (iii) mode beating (Breger 2000; Bowman et al. 2016), and (iv) non-linear mode coupling (Breger & Montgomery 2014; Bowman et al. 2016; Zong et al. 2016b,a).

For the specific case of close binary systems, the changing viewing aspect of a pulsation mode, throughout an orbital period, can also introduce pulsation amplitude changes. For example, TPPs can show amplitude changes on timescales commensurate with the orbital period, but the average amplitude over one orbit compared to the next does not change. However, if the geometrical configuration of TPPs (e.g., surface distribution and viewing angle) changes due to the evolution of the orbit (i.e. precession), one can expect to see amplitude variations of TPPs over a longer time period. This possibility has been demonstrated in TPP models where amplitudes of TPPs change with a change in viewing inclination (see figure 10 in Zhang et al. 2024).

V453 Cyg (α=20:06:34.97, δ=+35:44:26.27) is a DLEB with a β Cep primary that shows pulsation amplitude variations in the newest observations obtained using the *Transiting Exoplanet Survey Satellite* (*TESS*; Ricker et al. 2015). V453 Cyg consists of two massive (> 8 M$_\odot$) stars and is a member of the young open cluster NGC 6871. The primary in V453 Cyg is beyond the halfway point of its main-sequence evolution (Pavlovski & Southworth 2009). V453 Cyg is the first β Cep star in an EB with direct mass measurements (Southworth et al. 2020; hereafter JS20). But V453 Cyg has different values of stellar masses reported in different studies. For example, Southworth et al. 2004 (hereafter JS04) reported the primary to be 14.36(20) M$_\odot$ while Pavlovski et al. 2018 (hereafter KP18) and Serebriakova et al. 2025 (hereafter NS25) reported the same to be 13.90(23) M$_\odot$ and 13.87(24) M$_\odot$, respectively. This difference in mass measurement becomes a problem when one compares the measured dynamical mass with the one expected from stellar evolution models. Mass discrepancies of 10 to 30 per cent between evolutionary masses and dynamical masses have been reported in KP18 and NS25. V453 Cyg has an eccentric orbit and also has apsidal motion, the precession of the line of apsides with time (Wachmann 1973). JS04 also obtained a weighted-average mean of the internal structure constants that measure the density concentration of both the primary and secondary star in V453 Cyg, making it an excellent candidate to understand stellar structure from both asteroseismic and apsidal motion studies.

We present a new analysis of V453 Cyg, using high-cadence space-based photometry and high-resolution binary-phase-resolved spectroscopy, and show that it is the first EB with a changing pulsation axis. In this paper, we also reanalyse the apsidal motion of V453 Cyg in section 3.1 and present new estimates of masses and radii in section 3.2. The pulsation analysis is presented in section 3.4. Finally, in section 4, we discuss the changing pulsation axis and the connection between other physical phenomena in the system. In section 5, we present our conclusion and discuss why V453 Cyg is a potential benchmark for calibrating not only stellar models but also the dynamics of massive stars.

2 OBSERVATIONS

2.1 Photometry and pulsation extraction

V453 Cyg (TIC 90349611) was observed by the *TESS* space mission in sectors 14, 15, 41, 54, 55, 74, 75, 81, and 82 with 2 min cadence. Before extraction of the light curve, we looked for any source of external contamination in the target pixel files (TPF) by using the code TPFPLOTTER[2] (Aller et al. 2020). TPFPLOTTER overlays nearby stars from the *Gaia* data release 3 (Gaia Collaboration et al. 2023) on the TPF. We found that V453 Cyg was the only star that is in the photometric aperture (Fig. 1) used by the *TESS* Science Processing Operations Center (SPOC; Jenkins et al. 2016) and also in *Gaia*. There was a star close to the SPOC aperture mask (see star 2 in Fig. 1), but it was four magnitudes fainter than V453 Cyg. Therefore, we proceeded to extract the simple aperture photometry (SAP) light curves generated by *TESS* SPOC, using the LIGHTKURVE[3] package (Lightkurve Collaboration et al. 2018).

For our pulsation analysis, we extracted the pulsation light curve from the SAP light curves by subtracting the binary signal using version 40 of the code JKTEBOP[4] (Southworth 2013). JKTEBOP fits the light curves by calculating the projection of each star as a sphere for the eclipse shapes and as a biaxial ellipsoid for calculating proximity effects. We initialised a binary model using the system parameters from JS20. We optimised the surface brightness ratio (J), sum of relative[5] radii ($r_1 + r_2$), radius ratio (k), eccentricity (e), argument of periastron (ω), orbital inclination (i), time of primary minima T_0, orbital period ($P_{\rm orb}$), and third light fraction (lf$_3$). We also kept the reflection, limb-darkening, and gravity-darkening coefficients free to optimize. Only the mass ratio (q) was fixed using values from JS20. The optimisation used the Levenberg-Marquardt algorithm to find the best-fitting model. At this stage, the residuals showed non-periodic instrumental trends. To avoid contamination of the pulsation frequency spectra by these instrumental trends, the pulsation light curves were cleaned by adding additional de-trending polynomials using JKTEBOP. This procedure was repeated for all nine sectors. Examples of the original light curves and the pulsation light curves

[1] Here we refer to amplitude variations that are not due to the Tseraskaya-Blažko effect, which is quasi-periodic with periods of order a few tens of days.

[2] https://github.com/jlillo/tpfplotter

[3] https://github.com/lightkurve/lightkurve

[4] https://www.astro.keele.ac.uk/jkt/codes/jktebop.html

[5] defined to be a fraction of the semi-major axis (a).

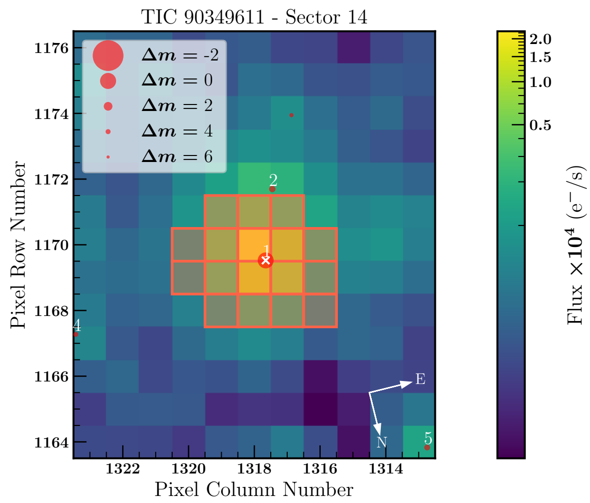

Figure 1. *TESS* TPF of V453 Cyg with nearby sources. The marker sizes indicate the magnitude difference between V453 Cyg and the respective star. The solid mesh marks the pixels used for the SPOC aperture.

for some sectors are shown in Fig. A1. Though JKTEBOP gives a precise fit, we only used it for the pulsation extraction and not the extraction of stellar parameters. This was because the distortion of the stars was substantial, and we needed a Roche model to get accurate parameters.

2.2 Spectroscopy and radial velocity extraction

We assembled and analysed spectroscopic observations of V453 Cyg with the high-efficiency and high-resolution Mercator Échelle spectrograph (HERMES; Raskin et al. 2011). HERMES provides a high resolving power ($R \simeq 85\,000$ at 550 nm) and a large wavelength coverage (approximately 380 to 1000 nm). We used 28 HERMES spectra of V453 Cyg, observed between 21st July 2021 and 4th August 2021, for our work. The reduction and the methods of the HERMES pipeline are described in detail in Tkachenko et al. (2024).

We used broadening functions (BF; Rucinski 1992) to extract radial velocities (RVs) from the HERMES spectra. Cross-correlation function (CCF) gives us repeated convolutions of the intrinsic broadening and amplifies the noise due to the intrinsic broadening. While BF uses Fourier transform to reduce the noise due to intrinsic broadening (see Rucinski 1999 for details). Therefore, BF gives us a better estimate of the stellar profiles than the CCF. We modified the single-order BF code, BF-RVPLOTTER[6], to calculate multi-order BFs. The BF was calculated over the wavelength range 4000-4700Å. We chose this segment as it had the highest density of narrow lines (along with the expected broad H and He lines) and lowest noise on the resultant BF. As our template, we used a synthetic spectrum generated with the code SPECTRUM using model atmospheres from ATLAS9, abundances from Asplund et al. (2009), and line lists from Randich et al. (2022). Based on the stellar parameters of the primary star from Pavlovski et al. (2018), the template created had a temperature of 28800 K, $\log g$ of 4.4 dex, [M/H] of 0 dex with projected rotational velocity ($v\sin i$) of 1 km s^{-1}. RVs of massive stars are affected by photospheric variability up to a contribution of 20 km s^{-1} (Sana et al. 2013). To clean the BFs of the noise due to this variability, we tested Gaussian smoothening filters with windows of 5, 10, 15, 20, and 25 km s^{-1}. We did not find any BF signal for filters with window of 5 and 10 km s^{-1}. All other filters were successful to generate a consistent BF signal with small fluctuations on the overall BF profile. Therefore, the final BFs generated were smoothed with a Gaussian smoother of a 15 km s^{-1} rolling window to avoid photospheric noise in the BF profile without over-smoothing RV variations.

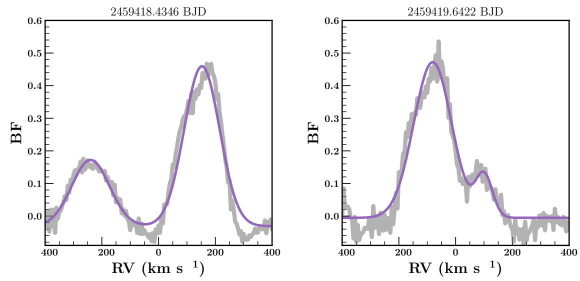

Figure 2. BF fits for two epochs of HERMES spectra. The two panels show the BFs for the widest (left) and the narrowest (right) RV separation measured in the spectra.

We fitted these BFs using a double Gaussian model and a non-linear least-squares minimisation method using the LMFIT[7] package (Newville et al. 2025). The fit was initialised with approximate Gaussian profiles for the primary and secondary. The primary was assigned a larger peak height and standard deviation with respect to the secondary. To aid the fitting process, we provided initial velocity estimates for the components by visual approximation. The final fitting routine fitted all the parameters of the double-Gaussian profile for both stars. An example of the BF fitting is shown in Fig. 2. The total errors on the obtained parameters were calculated using the correlation matrix of the RV fit (Wolberg 2006). We found a few spectra near the eclipses that had severely blended BF profiles, and hence we removed them from our subsequent analysis. The final 20 RVs are presented in Appendix B.

3 ANALYSIS

3.1 Orbital ephemeris and apsidal motion

The *TESS* data spanned over 1874 d or around 5.13 yr. We reevaluated the orbital ephemeris of the system using eclipse timings for both primary and secondary eclipses. We extracted eclipse minimum times using the morphological fitting code of Marcadon & Prša (2024). We combined these timings with eclipse times from JS04. A linear fit to the data gave the ephemeris,

$$T_{\rm min,pri} = 3.889821(2)\ {\rm d} \times E + 2458684.2080(9)\ {\rm BJD} \quad (1)$$

$$T_{\rm min,sec} = 3.889815(1)\ {\rm d} \times E + 2458684.15317(2)\ {\rm BJD}, \quad (2)$$

where E is the cycle number with the first eclipse observed with *TESS* being E=0. The residuals of the fit for primary and secondary indicated the presence of apsidal motion.

The apsidal motion in V453 Cyg was first detected by Wachmann (1973). The most recent study of V453 Cyg that addressed the apsidal

[6] https://github.com/mrawls/BF-rvplotter

[7] https://lmfit.github.io/lmfit-py/

Table 1. Apsidal motion parameters found in the current work compared to those found by JS04.

	This work	JS04
$\dot{\omega}$ [deg d^{-1}]	0.0114 ± 0.0010	0.0149 ± 0.0004
ω_0 [deg]	162 ± 5	309.7 ± 3.1
e_0	0.02354 ±0.00033	0.022 ± 0.002
T_0 [BJD]	2458684.2080 (fixed)	2439340.1036 ± 0.0019
$P_{\rm apsidal}$ [yr]	87 ±9	66.4 ± 1.8

motion was JS04, where the system was found to have an apsidal motion period of $U = 66.4 \pm 1.8$ yr, corresponding to an apsidal motion rate of $\dot{\omega} = 0.0149 \pm 0.0004^\circ\ d^{-1}$. Here, we reanalysed the apsidal motion using the recent *TESS* data. We calculated the apsidal motion using the methodology used in Rosu et al. (2022b) where we used the phase difference between primary and secondary eclipses, which is defined as

$$\Delta\phi_{\rm apsi} = \frac{T_2 - T_1}{P_{\rm ecl}}\,, \tag{3}$$

where $P_{\rm ecl}$ is the instantaneous sidereal period, the time interval between two consecutive primary minima. Using both the *TESS* time stamps and the time stamps from JS04, we calculated these variations for eclipses in the same binary period cycle. The values of $\Delta\phi_{\rm apsi}$ from the TESS data showed a scatter of 0.00034(1) throughout the sectors. We attributed this scatter to the stellar pulsations.

To avoid any possible numerical bias due to this scatter of data points, we binned the $\Delta\phi_{\rm apsi}$ from closely spaced *TESS* sectors (14-15, 41, 54-55, 74-75, and 81-82) to get five data points. The $\Delta\phi_{\rm apsi}$ variations were then fitted using the relation from Giménez & Bastero (1995) of

$$\Delta\phi_{\rm apsi} = \frac{1}{2} + A_1\frac{e}{\pi}\cos\omega - A_3\frac{e^3}{4\pi}\cos 3\omega + A_5\frac{e^5}{16\pi}\cos 5\omega\,, \tag{4}$$

where A_1, A_3, and A_5 are functions of e and i. The time variability of ω and apsidal motion was introduced in Eqn. (4) by considering that $\omega = \omega_0 + \dot{\omega}(t - T_0)$, where ω_0 is the argument of periastron at a reference time T_0, which we set to the first *TESS* minima, as calculated earlier. We also assumed that e_0 is the eccentricity at T_0 and does not change with time. Therefore, the variables in our apsidal motion fitting were ω_0, $\dot{\omega}$, and e_0.

This method was beneficial as we could select the eclipse times from the same orbital cycle, and therefore we did not have to worry about changes due to the light travel time effect and differences in the systematics of timing estimation between observers, if any. We estimated the best-fitting model using the Nelder-Mead method (Nelder & Mead 1965). We then sampled the errors using the Markov Chain Monte Carlo (MCMC) method with 100 walkers, 1500 steps, and a burn-in of 500 steps. The parameter distribution of the MCMC chains is shown in Fig. 3, and the fit is shown in Fig. 4. Our estimates showed a slower apsidal motion rate, compared to JS04, while the eccentricity values were consistent within the errors. The comparison of apsidal motion parameters in our work and JS04 is shown in Table 1.

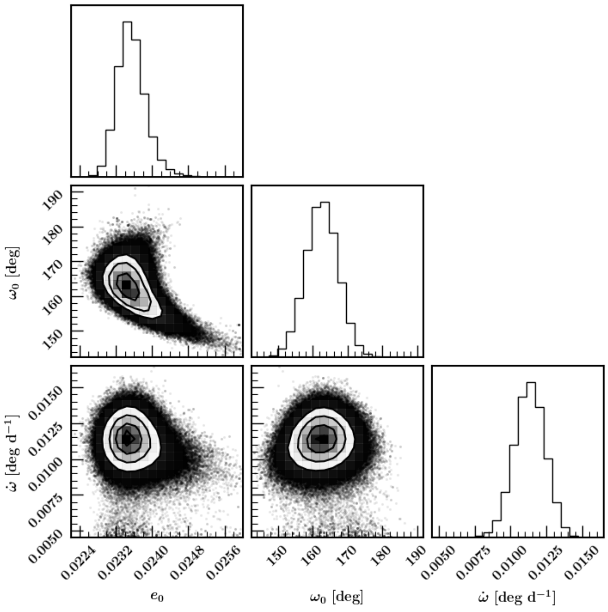

Figure 3. Corner plot for the MCMC chains of the apsidal motion fit.

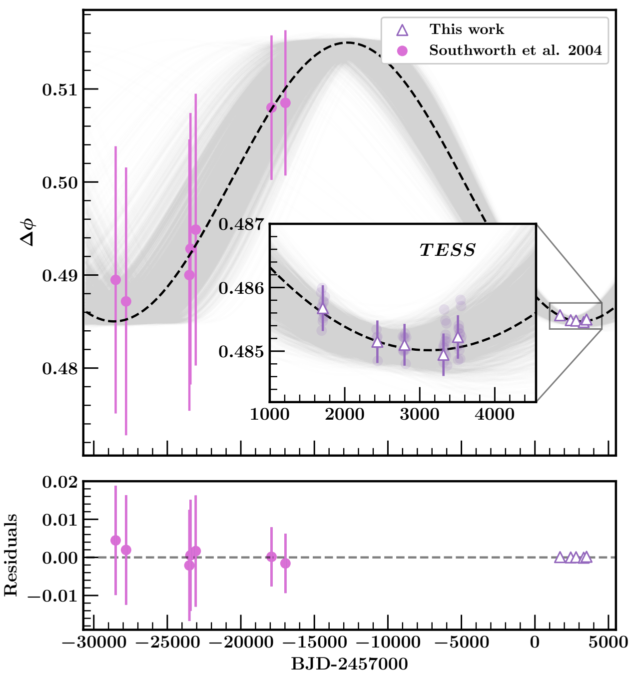

Figure 4. Fitting for the difference of minima times of consecutive primary and secondary eclipses. The hollow triangles represent *TESS* measurements binned by sets of consecutive sectors. The filled dots represent observations taken from JS04. The dashed black lines represent the best-fitting model for apsidal motion. The grey lines represent the different models from the MCMC chains.

3.2 Stellar parameters

The HERMES spectra used in our study coincided in time with *TESS* sector 41. The total span of the combined observations was around 28 d which corresponded to a change in ω of 0.3°. This provided us with an opportunity to simultaneously model the RVs and the light

Table 2. PHOEBE2 setup, and priors used for the MCMC solution. The setup includes the PHOEBE2 parameters corresponding to the limb darkening, reflection effect, gravity darkening, passband luminosity, and orbital precession rate. The priors are included from the spectroscopic estimates from KP18 and our apsidal motion analysis. More details about the PHOEBE2 parameters are available at: https://phoebe-project.org/docs/2.4/physics.

Parameter	Value
Fixed parameters	
`ld_mode`	'logarithmic'
`ld_coeffs@primary`	[0.144, 0.065]
`ld_coeffs@secondary`	[0.108, 0.074]
`irrad_method@compute`	'horvat'
`irrad_frac_refl_bol`[a]	1
`gravb_bol`[a]	1
`pblum_mode`	'component-coupled'
`dperdt`	0.0114 deg d^{-1}
Priors	
P_{orb}[d]	3.889818±0.000001
$T_{0,supconj}$ [TBJD]	1684.2080±0.0009
e	0.02354 ± 0.00033
$T_{eff,1}$ [K]	28800 ± 1000
`syncpar@primary`	0.96 ± 0.1
`syncpar@secondary`	1.4 ± 0.4

[a] For all components

curves for V453 Cyg, without any significant discrepancies arising as a result of the apsidal motion. We used version 2.4.17 of the public PHOEBE2 binary modelling software[8] (Prša et al. 2016; Horvat et al. 2018; Jones et al. 2020; Conroy et al. 2020) as it uses a Roche model, which is needed for close binaries. For computational efficiency, we used a resampled light curve after removing the dominant pulsation using a sine fit. The resampled light curve consisted of 1000 points from the eclipse phases and 400 from the out-of-eclipse phases. We converted the radial velocities to the *TESS* BJD time format before including them in the PHOEBE2 model.

We initialised our model using the WD2004 solution obtained in JS20. We fixed the period (P_{orb}), T_0 (which is the parameter $T_{0,supconj}$ in PHOEBE2), e, and $\dot{\omega}$ from the analysis in Section 3.1. The data for the simultaneous light curve and RV model were around 740 d ahead of the T_0 assigned, corresponding to a change in ω of 8° due to the apsidal motion. But our PHOEBE2 model has $\dot{\omega}$ assigned, so it automatically calculates ω at the corresponding data points. We used a logarithmic limb-darkening law and initialised the coefficients from Claret (2017). For modelling these hot stars, we used the PHOEBE2 suggested values of 1 for the reflection effect and gravity darkening, for both components. The irradiation model was set to the Horvat scheme (Prša et al. 2016). The parameters used in the PHOEBE2 setup are given in Table 2.

We optimised the initial model by selecting different combinations of free parameters in successive iterations. The parameters that were included in the combinations were $r_1 + r_2$, k, i, masses of the components (M_1 and M_2), systemic velocity (v_γ), passband luminosity of the primary ($L_{pb,1}$), and the effective temperature ratio between the secondary star and the primary star (T_{ratio}). Each combination of free parameters was optimised by using 100 iterations of the Nelder-Mead algorithm. We optimised the model until the root-mean-square

[8] https://phoebe-project.org/

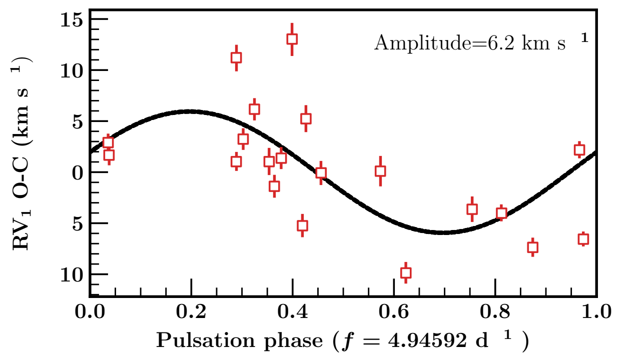

Figure 5. Residuals of the primary, after subtraction of the initial PHOEBE2 model from the RVs, phased to the dominant pulsation frequency. The black line represents the best-fit sine function.

(rms) of the residuals was less than one per cent. We then optimised the limb-darkening coefficients and updated them in our PHOEBE2 setup (Table 2). In this optimised solution, we noticed a scatter in the RV residuals. We found that the RV residuals of the primary star varied sinusoidally with an amplitude of 6.2 km s^{-1} and had the same frequency as that of the dominant frequency (Fig. 5). To improve the binary model, we removed this signal from the primary RV before sampling the binary solution for the final solution. We cannot identify a similar signal (corresponding to pulsations) for the secondary.

We used the MCMC algorithm implemented in PHOEBE2 to sample around the best-fit Nelder-Mead solution. We set a Gaussian prior for the fixed parameters: primary temperature, e, ω, P_{orb}, and $T_{0,supconj}$. To accommodate any variation over time, we used a uniform prior for the PHOEBE2 synchronicity parameters, using the spectroscopic solutions in KP18. The priors used in our PHOEBE2 setup can be found in Table 2. We started the sampling from Gaussian distributions around the following optimised parameters: $r_1 + r_2$, k, i, ω, M_1, M_2, γ, $L_{pb,1}$, and T_{ratio}. We also kept the absolute third light (l_3) free to sample for any errors due to it. The MCMC consisted of 60 walkers and 3500 iterations. We set 2000 iterations for burn-in (corresponding to 20 times the autocorrelation time of the chain) and used the remaining 1500 iterations for our parameter estimate. The MCMC sampled parameters and their corresponding corner plot is presented in Appendix C. The final adopted set of absolute parameters, after propagating through constraints, is presented in Table 3. The final model fit is shown in Fig. 6. Hereby, we refer to this solution as the joint solution.

The light curve residuals during the secondary eclipse suggest the possibility of additional orbit-synchronised pulsations. Meanwhile, in the residuals of the RV fit, we saw the residuals of the secondary RV varying between 5 and 25 km s^{-1}. These variations were higher than expected from gravitational redshift, which only contributed to a shift of around 1.5 km s^{-1} in the secondary RV. Therefore, we attributed these variations in residuals to a combination of stellar pulsations and microturbulent velocity changes (Markova et al. 2025).

We also found that the joint solutions give us a precise ω = 158.67(61), which is consistent with the one obtained from apsidal motion analysis.

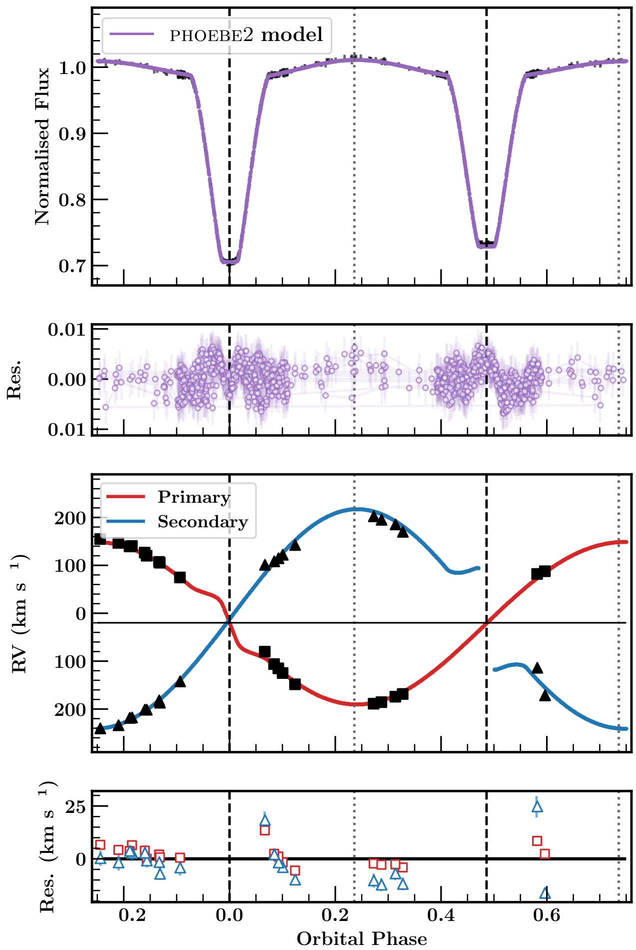

Figure 6. The final PHOEBE2 model fits (after MCMC) to the *TESS* sector 41 light curve (topmost panel) and the RVs (second panel from the bottom) of V453 Cyg. The narrow panels below them show the residuals of the fits. Squares and triangles represent the primary and secondary RVs, respectively. The primary RVs shown here are corrected for the signature of the dominant pulsation.

Table 3. Adopted orbital and stellar parameters for V453 Cyg.

	Orbital Parameters	
	Aa	Ab
T_0 [BJD - 2450000]	1684.2080(9)	
$P_{\rm orb}$ [d]	3.889818(1)	
a [$R_\odot$]	30.702(75)^a	
e	0.02354(33)	
i [deg]	87.27(28)	
ω_0 [deg]	158.67(61)	
K [km s^{-1}]	172.6(3)^a	226.4(9)^a
	Stellar and atmospheric parameters	
M [$M_\odot$]	14.56(13)	11.103(65)
R [$R_\odot$]	8.575(32)	5.378(30)
$T_{\rm eff}$ [K]	28800(500)^b	27930(486)^a
$\log(g)$ [dex]	3.7349(25)	4.0221(49)
$\bar{k}_2$	0.0046(5)	
	System parameters	
v_γ [km s^{-1}]	-17.35(22)	
lf_3	0.046(9)	
Age [Myr]	9.9 - 10.4	

^{a} Propagated from MCMC solution. ^{b} From KP18.

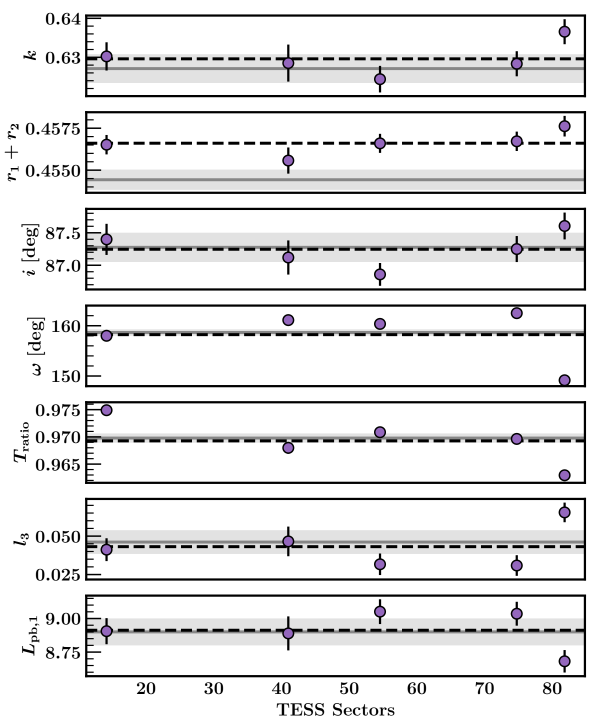

Figure 7. Variation of light curve solutions over different *TESS* sectors. The dashed line represents the mean of the light curve solutions. The grey line and the shaded area represents the mean and errors of the joint solution, respectively.

3.2.1 Consistency of the solution

While we did not have RVs for joint solutions in all *TESS* sectors, we used the remaining sectors to test the consistency of our solution. We calculated a separate set of solutions using light curves from combined sectors 14-15, 54-55, 74-75, and 81-82. Details of the calculations can be found in Appendix C. We also optimised sector 41 using this setup to check for any significant offsets from the joint solution. We found that the light curve solutions differ slightly ($\leq 3\sigma$) from the joint solution, with only $r_1 + r_2$, and $T_{\rm ratio}$ showing significant discrepancies. ω also showed variation over *TESS* sectors, but even with the sector-wise variations, the mean of the respective parameters over the sectors was within the 1σ error bars of the joint solution. The only exception was $r_1 + r_2$, where the mean of the light curve solutions was $\sim 3\sigma$ away from the joint solution. But the $r_1 + r_2$ values from the light curve solution are stable, with a standard variation of only 0.15 per cent from their mean. We note that $r_1 + r_2$ and $T_{\rm ratio}$ are sensitive to the eclipse geometry that is affected by pulsations here. Therefore, we endorse a joint (simultaneous RV and light curve) solution to get accurate parameters.

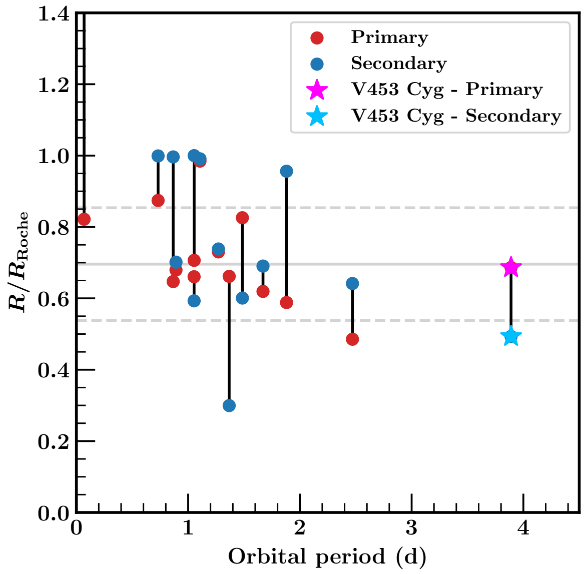

Figure 8. Roche-filling factors (R/R_{Roche}) versus orbital periods for TPPs with mass and radius measurements in the literature. V453 Cyg is marked with a star. The grey lines show the mean (solid) and standard deviation (dashed) for the Roche-filling factors of all pulsators in the sample.

3.2.2 *Roche deformations and tidal perturbations*

V453 Cyg has substantial Roche deformation. Fuller et al. (2020) showed that the tidal perturbation of pulsations is dependent on the pulsating star's Roche-filling factors (R/R_{Roche}). Using the masses and radii of the stars, we checked for the possibility of TPP on either of the stars in V453 Cyg. Figure 8 shows the R/R_{Roche} of V453 Cyg versus TPPs from the literature that have mass and radius measurements (Appendix D). The primary of V453 Cyg lies near the mean R/R_{Roche} (0.69±0.16) of this sample of 13 TPP systems. By treating this mean R/R_{Roche} as an empirical limit for hosting TPP, our binary analysis confirmed the conclusion of JS20, who reported TPPs in the primary pulsating star of V453 Cyg. Meanwhile, based on this R/R_{Roche} limit, we did not expect the pulsations on the secondary to be tidally perturbed, if present.

3.3 Internal stellar structure constants

Apsidal motion can give us an insight into V453 Cyg's stellar structure, complementary to the asteroseismic insight. Using the apsidal motion parameters, we can calculate the internal structure constant (k_2), which describes the distribution of mass from a star's centre to its surface (Hejlesen 1987; Sirotkin & Kim 2009). The apsidal motion rate of a binary is usually a contribution of two terms arising from different effects

$$\dot{\omega} = \dot{\omega}_{\mathrm{N}} + \dot{\omega}_{\mathrm{GR}} \, . \tag{5}$$

The apsidal motion rate measured in Sect. 3.1 is dominated by the Newtonian contribution $\dot{\omega}_{\mathrm{N}}$ which amounts to $0.0109 \pm 0.0010\,\mathrm{deg\,d^{-1}}$, over the general relativistic contribution $\dot{\omega}_{\mathrm{GR}}$, which amounts to $0.000492 \pm 0.000006\,\mathrm{deg\,d^{-1}}$, as calculated using equations (11) and (12) in Rosu et al. (2022a). We further used equation (13) of Rosu et al. (2022a) to define a weighted-average mean of the internal stellar structure constants of the stars:

$$\bar{k}_2 = \frac{c_1 k_{2,1} + c_2 k_{2,2}}{c_1 + c_2} = \frac{\dot{\omega}_{\mathrm{N}}}{c_1 + c_2}, \tag{6}$$

where $k_{2,j}$ is the k_2 of star j and c_j are a coefficient that only depends on observed properties of the stars. The calculated value of $\bar{k}_2$ is given in Table 3.

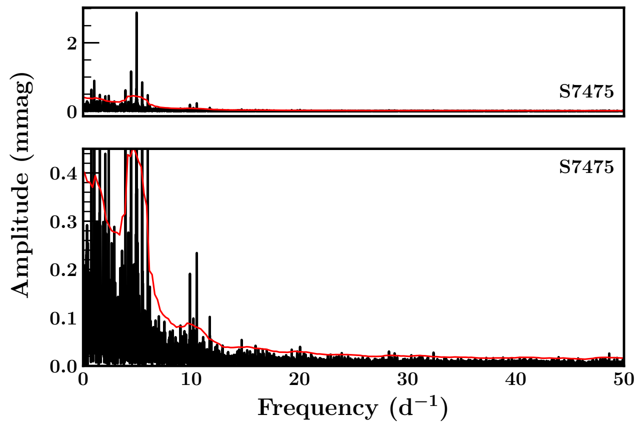

Figure 9. The full regime of DFT of the pulsation light curve for sector segments 74-75. The red lines show the S/N limit of 3.

3.4 Frequency analysis

The pulsation light curves showed amplitude variations over different *TESS* sectors (Fig. A1). To constrain these variations, we used four sets of consecutive sectors because a single sector was not sufficient to detect these varying pulsations with significance. We extracted the pulsation frequencies separately for these sector segments, where each segment consisted of two consecutive sectors: 14-15, 54-55, 74-75, and 81-82. Before the extraction, we subtracted the T_0 of the EB from the time series to get phase solutions in one reference frame. We used PERIOD04[9] (Lenz & Breger 2005) for our frequency extraction. PERIOD04 uses the discrete Fourier transform (DFT) to create frequency spectra from the pulsation light curves. We used iterative pre-whitening to extract frequencies from the frequency spectra. The frequency fitting involved the Levenberg-Marquardt non-linear least-squares procedure. According to Baran & Koen (2021), two sectors of *TESS* 2 min cadence data can detect a signal with the signal-to-noise ratio (S/N) of 5.1 with a false alarm probability of 0.1 per cent. Our frequency extraction procedure looked below this limiting S/N of 5.1 for any low-amplitude sidelobes of any potential multiplets indicative of TPPs (e.g. Jayaraman et al. 2022), restricting only to an S/N of 3. As expected, the resultant frequency spectrum varied over the sector segments. New frequencies were visible in some segments, and some frequencies disappeared. We also found that there were no significant frequencies beyond $50\,\mathrm{d^{-1}}$, and hence we restricted our further analysis to below this regime (Fig. 9).

For calculation of our varying frequency solution, we first obtained an initial solution for segment 81-82 as it showed the most frequencies. We then used it as the trial solution for all other sector segments

[9] https://www.period04.net/

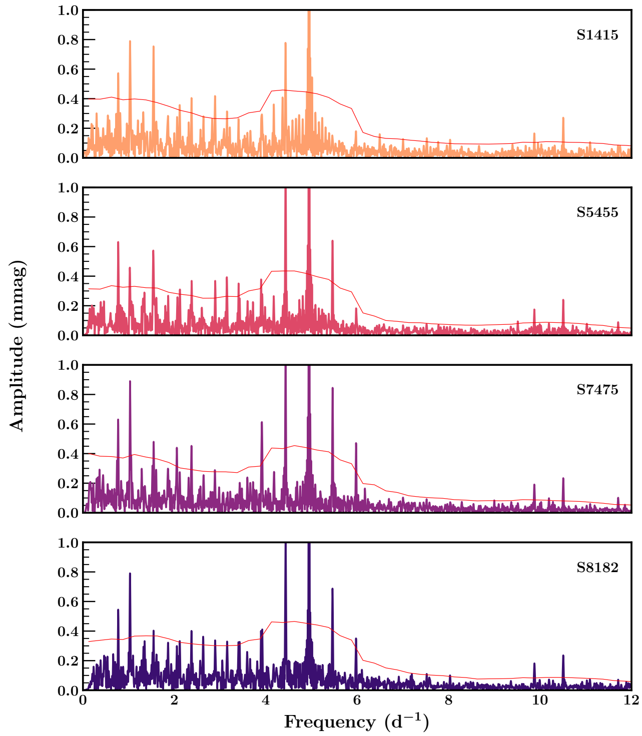

Figure 10. DFTs of *TESS* light curves for different sector segments. The red lines show the S/N limit of 3. The amplitude variations are prominent in the frequencies between 1 d^{-1} and 6 d^{-1}.

only avoiding frequencies that were below the S/N of 3 in the DFTs of the respective sector segments. We calculated a frequency solution for each sector segment independently, with the frequency, amplitude, and pulsation phase free during the fitting process. These fits gave us a solution only for the frequencies common to all sector segments. Further, for each sector segment, we extracted additional frequencies until the respective S/N limit was reached. This final frequency solution was the complete solution for each sector segment. The uncertainties on the amplitude and phase were calculated using MCMC sampling on the complete solutions of each sector segment. We found 10 frequencies common to all the sector segments. 14 frequencies were found in two or three sector segments. We rejected all frequencies that were only significant in one sector segment. The final list of all the extracted frequencies is given in Table 4. The value of individual frequencies varied over the sector segments but not more than 0.015 d^{-1}, and therefore we list averaged frequencies in the table. The full table can be found in the online version of the manuscript. The most prominent frequencies were observed below 12 d^{-1}. The frequency spectra variation for different sector segments is shown in Fig. 10. We also searched for combination frequencies and found that several frequencies are combination of f_{12} and $f_{\rm orb}$, given that the tolerance limit is three times the frequency errors (see remarks in Table 4). Most of these frequencies are either tidally perturbed pulsations or spatially filtered (see next subsection for details). Some higher frequencies can also be represented as a combination of f_{12} and $f_{\rm orb}$ but with very large coefficients.

We also calculated a fixed-frequency solution for all sector segments (see Appendix E) and ruled out any degeneracy between frequency variation, amplitude, and phase variation observed in the system. We found that amplitude variations were consistent in both the solutions.

3.4.1 Classifying pulsations

To get a complete picture of these pulsation variations, we classified the extracted frequencies. We classified them by comparing the amplitudes of the frequencies in five different versions of the light curves. The first version was the out-of-eclipse (eclipse data points removed) portion of the initial light curve. This light curve contains both binary and pulsation signatures. We called this LC1. The second consisted of the out-of-eclipse portion of the pulsation light curve. We called this LC2. The third was the pulsation light curve without primary eclipses. We called this LC3. The fourth was the pulsation light curve during the primary eclipses only. We called this LC4. The fifth and final was the pulsation light curve during the secondary eclipses only. We called this LC5. Figure 11 shows these diagnostic light curves phased to the orbital period along with their corresponding periodograms.

If a frequency is large in amplitude (compared to other frequencies in the same periodogram) in LC4 but not in LC2, LC3, and LC5, then it is likely subject to spatial filtration[10] on the primary star (Aerts et al. 2010; Bíró & Nuspl 2011; Johnston et al. 2023). There were eight spatially filtered frequencies in our frequency solution: $f_4, f_5, f_6, f_7, f_8, f_9, f_{15}$, and f_{16}.

There were five frequencies visible in all light curve versions LC1 to LC5. These five frequencies, $f_{10}, f_{11}, f_{12}, f_{13}$ and f_{14}, were separated by a frequency spacing (Δf) equal to twice the orbital frequency ($f_{\rm orb}$). We classified these frequencies as TPPs. We discuss these frequencies in detail later in section 3.4.3.

There were three significant frequencies below 2 d^{-1}. The frequency f_2 was high in amplitude in LC1 and visible in all light curves except LC4. For this reason, we expected that it was due to the reflection effect (Napier 1968) from the secondary or an artefact from improper modelling of the stellar deformations. Whereas the other two low frequencies, f_1 and f_3, appeared in LC1 to LC5 and thus could be gravity-mode frequencies or due to comparatively small imperfections in the light curve model. But we could not resolve their origin with the current observations.

The rest of the frequencies in our frequency solution were unclassified due to low amplitudes or inconsistent signals in these diagnostic light curves. It is also possible to deduce whether a frequency originates from the secondary. If a frequency is significant in LC2, LC3, and LC4 but not in LC5 (a total eclipse), then it arises from the secondary star. Using this rule, we identified one frequency originating from the secondary (see f_{19} in Table. 4).

3.4.2 Amplitude variations

We calculated the amplitude change (ΔA) of each frequency relative to the values in sector segment 14-15. We plot these variations in Fig. 12, for the different classifications described in the previous subsection. We found that the amplitude variation of certain TPP frequencies (e.g., f_{12} and f_{13}) were anti-correlated to the others (Fig. 12, top most panel). This ruled out amplitude change due to light dilution and hinted at the possibility of changes in the mode geometry of the TPPs. This explained the correlated changes for spatially-filtered frequencies (prominently f_8 and f_9) due to a change in the

[10] eclipse mapping is the method of identifying pulsation modes that are subject to spatial filtration in EBs.

Table 4. Extracted pulsation frequencies (averaged) with their amplitudes and pulsation phases for different datasets. The orbital harmonic of the system is $f_{\rm orb} = 0.257083(33)$ d. The values of frequencies (f_i), amplitudes (A_i), and phases (ϕ_i) are stated considered the fitting formula: $\sum A_i \sin(2\pi(f_i t + \phi_i))$. The classification of the frequencies are also reported: TP for TPP multiplets, BIN for binary signature, SEC for pulsation originating from the secondary, and SF for frequencies due to spatial filtering. The full table, with calculated frequencies for each sector segment, is available as supplementary material in the online version.

		Sectors 14-15		Sectors 54-55		Sectors 74-75		Sectors 81-82		
No.	$f_{\rm avg}$ (d^{-1})	A (mmag)	ϕ (rad)	A (mmag)	ϕ (rad)	A (mmag)	ϕ (rad)	A (mmag)	ϕ (rad)	remarks
f_1	0.7704(7)	0.60(1)	0.659(3)	0.624(9)	0.312(2)	0.63(1)	0.823(2)	0.537(9)	0.301(3)	-
f_2	1.0282(6)	0.86(1)	0.009(2)	0.440(9)	0.012(3)	0.87(1)	0.568(2)	0.789(9)	0.007(2)	BIN; $4f_{\rm orb}$
f_3	1.5432(8)	0.77(1)	0.983(2)	0.566(9)	0.783(3)	0.47(1)	0.131(3)	0.406(9)	0.006(4)	$6f_{\rm orb}$
f_4	2.118(1)	0.35(1)	0.693(5)	0.307(9)	0.138(5)	0.27(1)	0.698(6)	0.323(9)	0.594(5)	$f_{12} - 11f_{\rm orb}$
f_5	2.375(1)	0.37(1)	0.620(5)	0.382(9)	0.151(4)	0.44(1)	0.395(4)	0.378(9)	0.743(4)	$f_{12} - 10f_{\rm orb}$
f_6	2.633(2)	0.24(1)	0.294(7)	-	-	-	-	0.335(9)	0.794(4)	SF; $f_{12} - 9f_{\rm orb}$
f_7	2.890(1)	0.42(1)	0.427(4)	0.390(9)	0.681(4)	0.29(1)	0.510(5)	0.335(9)	0.654(4)	$f_{12} - 8f_{\rm orb}$
f_8	3.146(3)	0.31(1)	0.996(6)	0.382(9)	0.701(4)	-	-	0.283(9)	0.030(5)	SF; $f_{12} - 7f_{\rm orb}$
f_9	3.428(2)	-	-	0.260(9)	0.241(6)	-	-	0.272(9)	0.746(5)	-
f_{10}	3.915(1)	-	-	0.257(9)	0.710(6)	0.58(1)	0.218(3)	0.400(9)	0.115(4)	TP; $f_{12} - 4f_{\rm orb}$
f_{11}	4.4315(4)	0.88(1)	0.907(2)	1.118(9)	0.766(1)	1.15(1)	0.498(1)	1.105(9)	0.941(1)	TP; $f_{12} - 2f_{\rm orb}$
f_{12}	4.9461(1)	3.11(1)	0.1466(6)	2.726(9)	0.9844(5)	2.87(1)	0.1422(5)	2.806(9)	0.2233(5)	TP
f_{13}	5.460(2)	-	-	0.541(9)	0.828(3)	0.82(1)	0.405(2)	0.743(9)	0.721(2)	TP; $f_{12} + 2f_{\rm orb}$
f_{14}	5.974(2)	-	-	-	-	0.43(1)	0.152(4)	0.389(9)	0.014(4)	TP; $f_{12} + 4f_{\rm orb}$
f_{15}	7.518(4)	0.12(1)	0.50(1)	-	-	-	-	0.086(9)	0.63(2)	SF; $f_{12} + 10f_{\rm orb}$
f_{16}	8.032(5)	0.11(1)	0.99(2)	-	-	-	-	0.091(9)	0.44(2)	SF; $f_{12} + 12f_{\rm orb}$
f_{17}	9.875(2)	0.16(1)	0.22(1)	0.181(9)	0.134(8)	0.19(1)	0.181(8)	0.177(9)	0.730(8)	-
f_{18}	10.507(2)	0.27(1)	0.115(7)	0.239(9)	0.690(6)	0.23(1)	0.334(7)	0.238(9)	0.935(6)	-
f_{19}	11.707(5)	-	-	0.092(9)	0.41(2)	0.09(1)	0.47(2)	0.083(9)	0.08(2)	SEC
f_{20}	19.53(2)	0.05(1)	0.09(4)	-	-	-	-	0.028(9)	0.79(5)	$4f_{12} - f_{\rm orb}$
f_{21}	19.79(1)	-	-	0.028(9)	0.74(5)	0.03(1)	0.91(5)	-	-	$6f_9 - 3f_{\rm orb}$
f_{22}	28.24(3)	-	-	-	-	0.03(1)	0.66(5)	0.007(9)	0.8(2)	$8f_{12} - 44f_{\rm orb}$
f_{23}	32.39(3)	0.04(1)	0.81(5)	-	-	0.02(1)	0.90(6)	-	-	$4f_{12} + 49f_{\rm orb}$
f_{24}	43.92(7)	0.02(1)	0.9(1)	-	-	0.01(1)	0.8(2)	-	-	$6f_{12} + 55f_{\rm orb}$

projected surface area that is being eclipsed by the secondary star (Fig. 12, second panel from top). The low-frequency pulsation that we attributed to the reflection effect, f_2, had a non-monotonic variation anti-correlated to spatially-filtered f_8 and f_9. The other two low-frequency pulsations, f_1 and f_3, showed monotonic or no variation (Fig. 12, third panel from top). All of the unclassified frequencies showed little variation in amplitude except f_{18}, f_{19}, and f_{20}. They were either invisible or had larger amplitudes in sector segment 14-15 compared to the other sector segments (Fig. 12, bottom panel).

3.4.3 *Tidally perturbed pulsations*

To understand the variations in the TPPs, we created échelle diagrams for all the sector segments. We found that three TPP frequencies, including the dominant pulsation, were at the same échelle phases (Fig. 13), indicating that they belonged to the same mode. These frequencies were separated by $\Delta f = 2f_{\rm orb}$. Two frequencies, f_{10} and f_{14}, had $\Delta f \sim 4f_{\rm orb}$ with respect to the dominant frequency. The échelle phases of f_{10} and f_{14} were similar to that of the dominant frequency but not the same. Both f_{10} and f_{14} “oscillated" around échelle phase of the dominant frequency, over the different sector segments (Fig. 13), with their échelle phases varying to a maximum of 6-σ and 3-σ away, respectively. It was still possible that these frequencies belonged to the dominant TPP mode if these échelle phase differences arose from any transitions that caused the pulsation amplitude variations. Therefore, we discuss the possibility of a TPP with both three- and five-frequency configurations in this paper. The conditions from Balona (2018) would make the TPP an $l = 2, m = 2$ mode if it was split into five frequencies (marked in blue in Fig. 13) or $l = 1, m = 1$ if it was split into three frequencies (marked in pink in Fig. 13).

We reconstructed the orbital runs of these multiplets: amplitude and phase variation of the mode over the orbital phase. We used the tidal perturbation model from Jayaraman et al. (2022). For a mode split into frequencies $f_{\rm mode} + nf_{\rm orb}$, with the corresponding amplitudes A_n and phases ϕ_n, the resultant amplitude C and phase Φ can be represented as function of the orbital phase $\phi_{\rm orb}$:

$$C(\phi_{\rm orb}) = \left[\left(\sum_n A_n \sin(2\pi[n\phi_{\rm orb} + \phi_n])\right)^2 + \left(\sum_n A_n \cos(2\pi[n\phi_{\rm orb} + \phi_n])\right)^2\right]^{\frac{1}{2}} \tag{7}$$

and

$$\Phi(\phi_{\rm orb}) = \frac{1}{2\pi} \arctan\left[\frac{\sum_n A_n \sin(2\pi[n\phi_{\rm orb} + \phi_n])}{\sum_n A_n \cos(2\pi[n\phi_{\rm orb} + \phi_n])}\right]. \tag{8}$$

We reconstructed two sets of orbital runs, considering that the mode consisted of three ($l = 1$) or five frequencies ($l = 2$). The left and middle panels in Fig. 14 represent the orbital runs for $l = 1$ and $l = 2$, respectively. We found that both $l = 1$ and $l = 2$ had extrema of amplitude variations at specific orbital phases. Both $l = 1$ and $l = 2$ were not perfect triaxial modes due to no characteristic phase variations of π at the eclipse phases (see Fuller et al. 2025). We saw a clear shift in the amplitude and phase extrema for both the

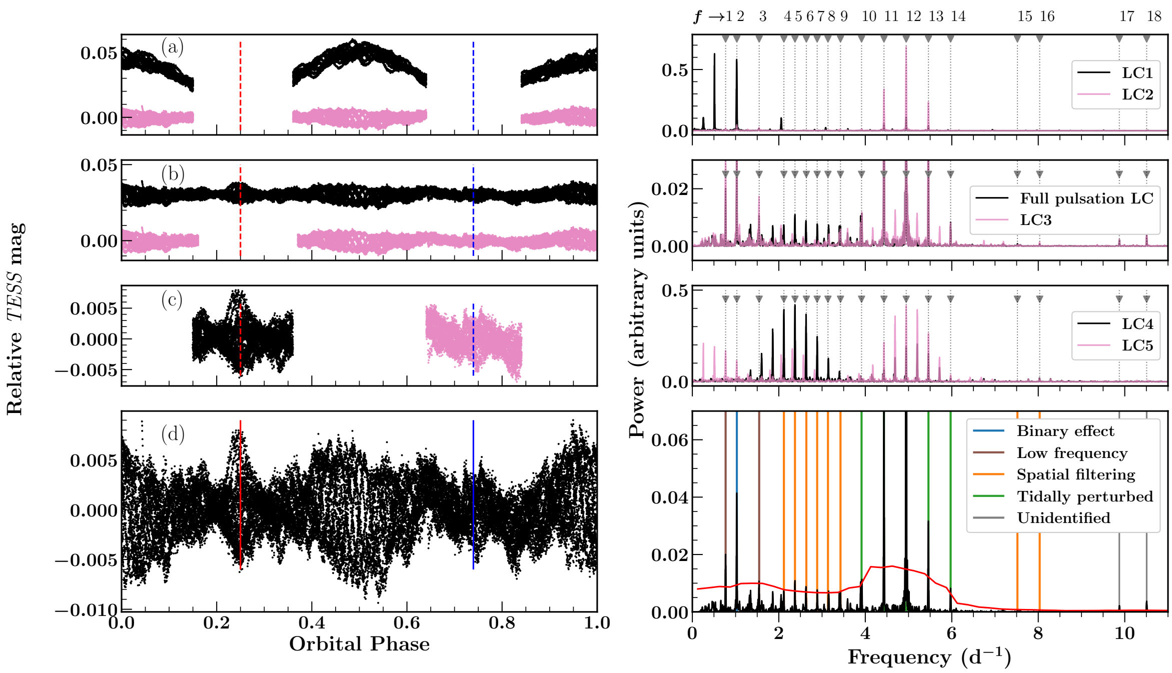

Figure 11. Diagnostic light curves (left panels) and their corresponding Lomb-Scargle periodograms (right panels) for *TESS* sectors 81 and 82. In the left panel, the dashed red and blue lines represent phases of primary and secondary eclipse, respectively. The grey vertical lines and the arrows in the right panels represent the final set of extracted frequencies. The bottommost panel on the right shows the classification of the identified frequencies. Blue vertical lines represent frequencies due to binary effects, brown vertical lines show other low-frequency modes, orange lines show spatially filtered frequencies, and green lines show TPP frequencies. The red line in the bottom right panel marks the S/N level of 3.

reconstructed modes over different sector segments. We compared these reconstructed orbital runs to the directly fitted orbital runs of the dominant f_{12} frequency. For the fitting, we followed an approach similar to Steindl et al. (2021). We divided the pulsation light curve into small segments that corresponded to 11 divisions of the orbital phase. We then fitted the small segments separately with the function

$$A(t) = A_0 \sin\left(2\pi(f_i t + \phi)\right) + c_0 \,, \tag{9}$$

where we fixed the frequency f_i, and fitted for the amplitude A_0, and ϕ of each segment, and c_0 is the zero-point shift in the amplitude of the fit. We used the Levenberg–Marquardt algorithm to fit for the parameters.

Though not as detailed as the reconstructed orbital runs, the observed orbital runs of the dominant frequency did capture the overall amplitude variations (Fig. 14, right plot). We found that the amplitude variation for f_{12} over the orbit was similar to that of the reconstructed l=2 TPP (see center plot in Fig. 14) only for sector segments 74-75. In each of the other sector segments, the profiles of the amplitude variation for the reconstructed runs and the f_{12} run were similar, but the maxima of these variations were shifted compared to one another. The phase variations for f_{12} showed extrema at specific orbital phases, but certain parts of the orbital runs were affected by degeneracy in phase fitting in small light curve segments. But all the orbital runs showed that the phase and amplitude extrema move around the eclipse phases over different sector segments. An extremum at a specific orbital phase is a result of an inclined pulsation axis (Zhang et al. 2024; Jayaraman et al. 2024; Fuller et al. 2025; Handler et al. 2025). Therefore, the variation of the amplitude and phase extrema possibly indicated a change in the orientation of the pulsating axis. We discuss this in detail in subsection 4.2.

4 DISCUSSION

4.1 Mass discrepancy

Our solutions predicted a higher mass for the primary compared to all other estimates in the literature (Table 5). Our estimates are the closest to JS04 even though other studies use newer spectra or, in NS25, the same sample of spectra. JS04 used RV modelling to get the spectroscopic orbit, unlike KP18 and NS25, where the estimate relied upon spectral disentangling. The reported RV semi-amplitudes are different, with K_1 slightly better behaved than K_2, hence, M_2 is better constrained than M_1. The difference could be a result of the line profile variations due to pulsations. NS25 found two different solutions depending on the set of free parameters. A fit with all parameters free in their setup, run (a), gave them lower binary masses and a lower primary radius. When they fixed e-related parameters in their setup, marked as run (b), they got higher masses and primary radii compared to run (a). The choice of e and ω could be crucial, given that the system has apsidal motion. In our trial solutions, we found that fixing l_3 to zero changed orbital inclinations and affected the primary mass estimation drastically. We also note that our estimated third light is higher than that obtained (or fixed) by JS20 and NS25 in their solutions, using *TESS* light curves. Therefore, treatment of third light could also be a source of the discrepancy. NS25 noted that

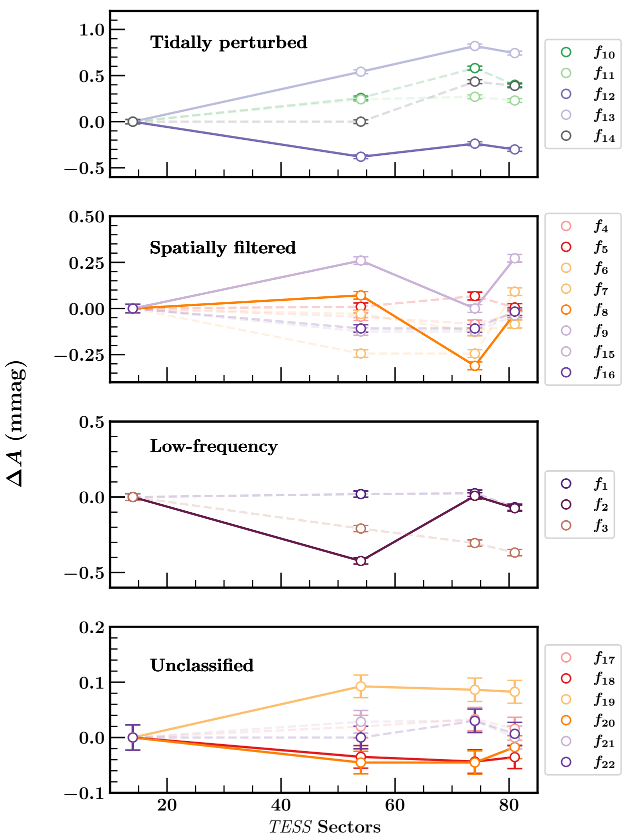

Figure 12. Amplitude variations of all extracted frequencies. The first panel (from the top) shows variations of frequencies of the TPPs. The second panel shows spatially-filtered frequencies. The third panel shows the low-frequency modes. The fourth and last panel shows the rest of the extracted frequencies. The amplitude variation of f_{12} and f_{13} are anti-correlated. f_8 and f_9 have correlated variations. The low-frequency f_2 has a non-monotonic variation. f_{18}, f_{19}, and f_{20} are the only unclassified frequencies showing any variation. The variation of these frequencies is highlighted with solid lines.

V453 Cyg has the largest observed mass discrepancy in their sample when compared to masses from stellar evolution models. JS04 did not report any mass discrepancy with stellar evolution models. Similarly, our values showed no strong indication of mass discrepancy compared with MESA isochrones (Dotter 2016; Choi et al. 2016) at solar metallicity, with a non-zero initial rotation ($v_{\rm ini}/v_{\rm crit}$ = 0.4), and with a 2.5 per cent uncertainty in age (Fig. 15). However, there is a need for a detailed study to validate the mass measurement methods and caution when comparing observed dynamic masses with stellar evolution models for massive stars.

4.2 Changing pulsation axis

We found that the dominant mode showed amplitude variations and orbital runs indicative of a change in mode geometry, possibly a changing pulsation axis. To show an actual change in the pulsation axis, we needed to calculate the extent of obliquity of the pulsation axis to the rotational axis of the primary star. Several cases of pulsation axis obliquity are found in the literature due to magnetic fields (see Kurtz 2022). Obliquity of a pulsation axis due to magnetic fields has been studied since the development of the oblique pulsator model (Kurtz 1982), which in addition to magnetic fields has also been used to study misalignment of pulsation axes due to tides (e.g. Handler et al. 2020; Rappaport et al. 2021; Handler et al. 2022; Fuller et al. 2025).

We used the oblique pulsator model to determine the obliquity β (i,e. the angle of the pulsation axis with respect to the rotational axis), assuming that the rotational axis was perpendicular to the orbital plane, i.e., inclined to the orbital axis. In our case, the tilt in the pulsation axis was because of the equilibrium tide acting in the orbital plane. A combination of the Coriolis force and the equilibrium tide can affect the amplitude ratios of the component frequencies of a tidally perturbed pulsation mode. These amplitude ratios are a function of β and orbital inclination i and are represented as

$$\gamma_m^-(\beta) = \frac{A_{l,m} - A_{l,-m}}{A_{l,m} + A_{l,-m}} \qquad \gamma_m^+(\beta) = \frac{A_{l,m} + A_{l,-m}}{A_{l,0}}, \tag{10}$$

where $A_{l,m}$ represents amplitudes of the $2m$+1 split frequencies in a mode with a given value of l (Bigot & Dziembowski 2002). These amplitude ratios are with respect to the central frequency and provide a relative measure of how β may vary in time.

Shibahashi & Aerts (2000) studied β Cephei, the prototype of the class, and showed that the amplitude ratio of the side peaks of a mode (i.e, ratio of γ_m^+) provides the exact value of β if one knows the inclination, i, of the system. For m=1,2 (i.e. there are five frequencies in the tidally split multiplet), this yields

$$\gamma_2^+/\gamma_1^+ = \frac{A_{2,2} + A_{2,-2}}{A_{2,1} + A_{2,-1}} = \frac{1}{4}|\tan i \tan\beta| \, . \tag{11}$$

Using Eqn. (11), we calculated the amplitude ratios for the TPPs for different sectors of TESS data for V453 Cyg. We found that the ratios vary over time, indicating a variable β (Fig. 16). Using i = 87.27 ± 0.27 deg obtained from our binary modelling, we calculated the values of β for the l = 2 case. We found that β increases by 5.1 deg across the 1620-d time span of the total TESS data set, as shown in Fig. 16. We then saw a decrease in β, which is indicative of the precession of the pulsation axis. If we assume that the time to reach the β maximum corresponds to a quarter of the full cycle, this suggests a precession period of about 17.6 yr.

4.3 Other plausible causes of amplitude variation

4.3.1 *Case of changing surface distribution*

In our frequency extraction, we did not enforce in the fitting f_{10}, f_{11}, f_{13} and f_{14} to be perfect integer multiplets of f_{12}, as these were extracted using the pre-whitening method. However, when we assumed these frequencies to be split by exact integer multiples of $f_{\rm orb}$ and then reconstructed the orbital runs, we found that the amplitude maxima were squeezed and stretched, which was most prominent in sector segment 14-15 (see Fig. 17). We postulate that this is the manifestation of a changing surface amplitude distribution of the mode. However, we do not have a physical explanation of why this would be the case. Nonetheless, the amplitude ratios of the multiplets obtained in this case still showed a changing β when modelled with the oblique pulsator model.

4.3.2 *Case of changing binary geometry*

Since the majority of massive stars exist in higher-order multiple systems (Sana et al. 2012; Offner et al. 2023), dynamical interactions are expected. Therefore, it is possible that the geometry of such a binary system is changing on a relatively short time scale,

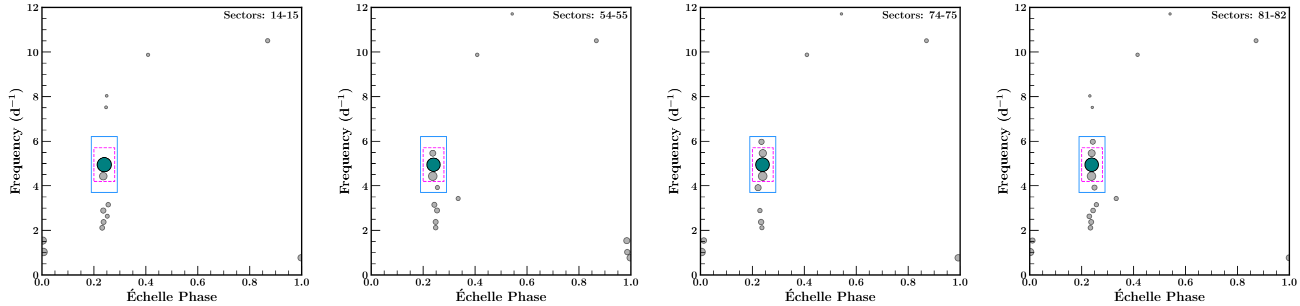

Figure 13. Échelle diagrams for the different sector segments. The échelle diagrams are calculated for the orbital frequency, $f_{\rm orb}$ = 0.2570814 d^{-1}, and the marker sizes are proportional to the amplitude of the frequencies. The colored boxes mark the potential multiplets of the dominant frequency.

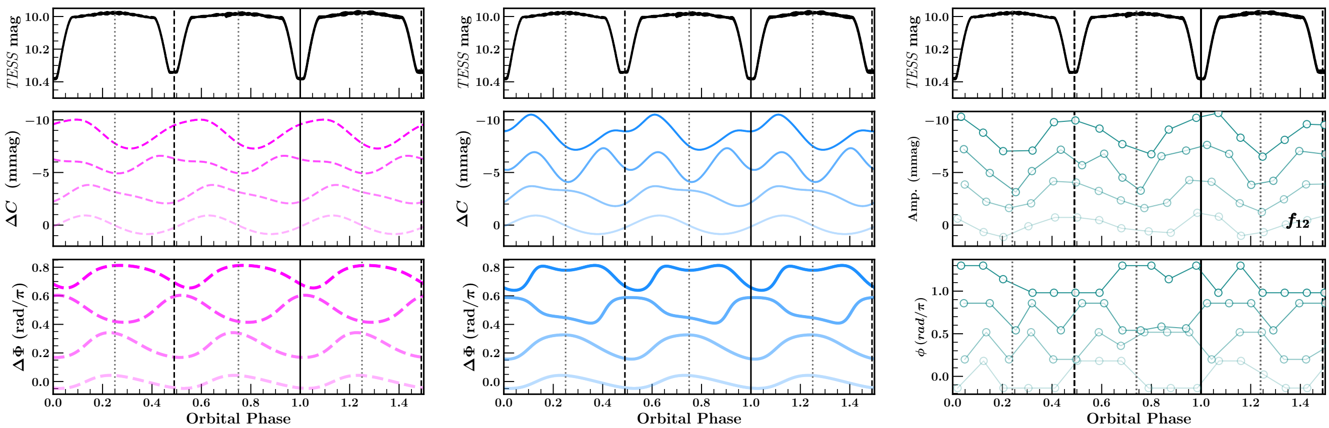

Figure 14. Orbital runs of the combined amplitude and phase of the combined TPPs and the dominant frequency. The left and middle panels show the reconstructed orbital run of the two possible configurations of the dominant mode, l=1 in pink and l=2 in blue. The right panel shows the orbital run of the dominant frequency f_{12} (in green) measured using the pulsation light curves. The green circles mark the amplitude and phase measurements of the light curve segments specific to an orbital phase. The line and marker opacity increases with increasing time (in *TESS* sectors).

Table 5. Masses, radii, and RV semi-amplitudes of V453 Cyg in the literature.

	M_1 [M$_\odot$]	M_2 [M$_\odot$]	R_1 [R$_\odot$]	R_2 [R$_\odot$]	K_1 [km s^{-1}]	K_2 [km s^{-1}]
JS04	14.36(20)	11.11(13)	8.551(55)	5.489(63)	173.7(8)	224.6(20)
KP18	13.90(23)	11.06(18)	8.62(9)	5.45(8)	175.2(13)	220.2(16)
JS20	13.96(23)	11.10(18)	8.665(55)	5.250(56)	175.2(13)^a	220.2(16) ^{a}
NS25 (a)	13.87(24)	10.93(29)	8.93(27)	5.56(11)	-	-
NS25 (b)	13.96(24)	11.37(29)	9.00(27)	5.58(11)	-	-
This work	14.56(13)	11.103(65)	8.575(32)	5.378(30)	172.6(3)	226.4(9)

^{a} Adopted from KP18.

which is affecting how we view the pulsations (e.g. Southworth et al. 2021). However, our analysis does not suggest that this is the case for V453 Cyg. For example, our binary solutions give us an inclination of 87.27 ± 0.28 deg, which does not vary substantially over all of the *TESS* sector segments spanning 1620 d (see Fig. 7). The other possibility is that the rotational axis is changing, but this would require a process faster than any usual rotational misalignment timescale (Albrecht et al. 2009, 2014; Southworth 2026). We looked at $v \sin i$ values in the literature to search for a changing rotational axis because a changing rotational axis would lead to different $v \sin i$ given that the system's inclination does not seem to vary. The literature $v \sin i$ values, for example, from JS04 and KP18, span several years and are consistent within their error bars. Furthermore, we did not find any phase and amplitude changes of the stellar pulsations at the spin precession frequency, which would be indicative of spin axis precession. A detailed check demands more spectroscopic data to study the Rossiter-McLaughlin effect (Rossiter 1924; McLaughlin 1924), which can help constrain the inclination of the stellar rotation axes with respect to the normal to the orbital plane.

Bigot & Dziembowski (2002) showed that the amplitude of variation of γ_m^- and γ_m^+ also depends on the strength of the perturbing field, which in our case would mean a change in the strength of the

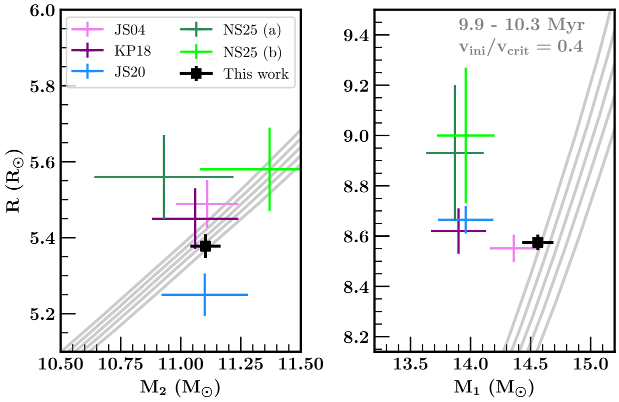

Figure 15. Mass and radius measurements in the literature compared against a set of MESA isochrones with ages between 9.9 and 10.3 Myr. The measurements obtained in this study are shown with filled squares.

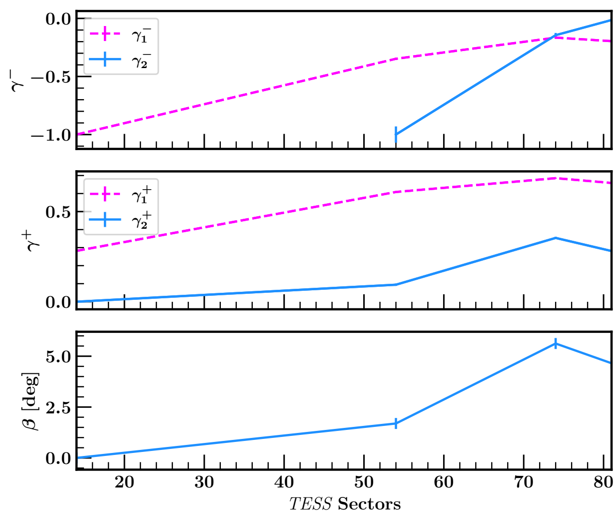

Figure 16. Amplitude ratio variations of frequencies of the dominant pulsation mode. Different panels show different amplitude ratios as defined in Bigot & Dziembowski (2002). The bottommost panel shows the variation of β calculated from the amplitude ratios. The error bars of the amplitude ratios are of the order of the line width, while errors on the β variation are clearly visible.

tidal torque. Such a change is effected by changes in the orbital separation. We do not see any substantial variation in the semi-major axis in our binary modelling. It could still be possible that there are minute variations in the semi-major axis and the amplitude changes in pulsation are the result of a combination of both changing orbit and changing pulsation axis. More simultaneous spectroscopic and photometric observations can probe this hypothesis.

4.4 Connecting physical processes

V453 Cyg seems to be a system in a transition state where several dynamical processes are occurring together. Whether these changes are interconnected is a question that needs to be explored. We used

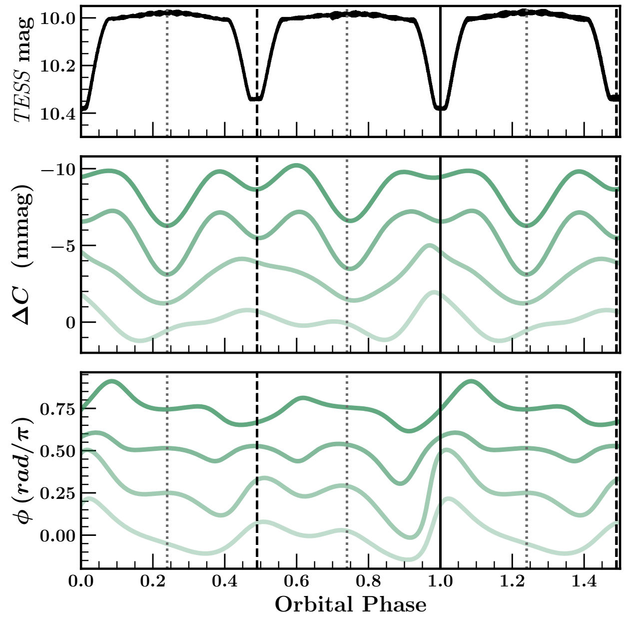

Figure 17. Orbital runs of the tidally split mode, assuming that the split frequencies are separated by perfect multiples of the orbital frequency.

the code JKTABSDIM[11] to calculate theoretical synchronisation and circularisation times using equations from Zahn (1975, 1977). We found that the expected synchronisation time for V453 Cyg was 3.06 ± 0.01 Myr and the circularisation time was 368 ± 8 Myr. According to the isochrones in section 4.1, the age of the V453 Cyg is about 10 Myr. Therefore, the system has only completed 3 per cent of its circularisation period. But it should have already synchronised. The delayed synchronisation opens up the possibility of inverse tides in V453 Cyg. Inverse tides are caused when the tidally forced mode amplitude is similar to the stable non-linear pulsation amplitude (Fuller 2021). This process causes the star to transfer energy to the orbit and pump it to a higher energy state. The current rotational velocity of V453 Cyg's primary is around 0.96 times the synchronisation velocity. Therefore, the inverse tides might have slowed the primary star to smaller spin frequencies, away from synchronisation. The slowing of stellar spins is expected to be accompanied by spin-orbit misalignment, which we have ruled out. But whether inverse tides can misalign, or actively change the misalignment of the pulsation axis in V453 Cyg is something to be explored in the future. The asynchronous rotation could also be a result of a "normal" binary evolution. This is because the calculations of synchronisation timescale vary in the literature, depending on the implementation of dynamical tides in the calculations (Sciarini et al. 2024). V453 Cyg can be used to further test these implementations.

We found that our estimates predicted a longer apsidal motion period compared to JS04. Our estimated apsidal motion period (~ 87 yr) is almost five times the tentative precession period of the pulsation axis. While this could be a coincidence, it highlights the need to use V453 Cyg as a laboratory to further test models and theories of tidal evolution of massive binaries.

[11] https://www.astro.keele.ac.uk/jkt/codes/jktabsdim.html

5 CONCLUSIONS

V453 Cyg is an eclipsing binary that exhibits β Cep pulsations with varying amplitudes. In this work, we used *TESS* photometry and HERMES radial velocities to obtain direct measurements of masses and radii of the components. The primary, the origin of the dominant pulsation, is a 14.56±0.13 $M_\odot$ star with a radius of 8.575±0.032 $R_\odot$. The secondary is also massive, with a mass of 11.103±0.065 $M_\odot$ and a radius of 5.378±0.030 $R_\odot$. The literature shows discrepancies in mass measurements, which we attributed to the choice of model parameters and technique for measuring orbital parameters. We found that the dominant pulsation is either an $l = 1$ or $l = 2$ mode, which is tidally perturbed and is changing its amplitude and phase over time. We attributed this variation to a changing pulsation axis that our analysis suggests is precessing with a period of about 17 yr and reaching a maximum obliquity of around 5 deg. The system also has apsidal motion with a rate of 4.1±0.4° yr^{-1}. This allowed us to estimate the weighted-average mean of the internal stellar structure constants, $\bar{k}_2 = 0.0046\pm0.0005$. Long-term monitoring of V453 Cyg, both spectroscopically and photometrically, is needed to constrain the mode and understand interactions of pulsations and tides.

V453 Cyg is an excellent potential benchmark for modelling many physical processes at work in massive stars. To accurately constrain a star's evolution, one needs information about its global properties and internal structure. Together with the precise masses and radii of both the primary and secondary stars, the dominant pressure mode and the $\bar{k}_2$ provide additional constraints for stellar evolution modelling. Indeed, the value of k_2 is linked to the density profile inside a star. In massive stars, the value of k_2 is especially sensitive to the region at the border between the convective core and the radiative envelope and is highly dependent on the amount of convective boundary mixing (Rosu et al. 2026). Meanwhile, pressure modes in β Cep stars are sensitive to interior rotation and mixing processes (Michielsen et al. 2019; Burssens et al. 2023; Vanlaer et al. 2025). Therefore, the constraints on the primary's pulsation mode can help us constrain the processes in the star's interior. Furthermore, V453 Cyg's orbital period is rather short and will enable one to test whether the system is experiencing tidally-enhanced or tidally-suppressed rotational mixing (e.g., Sciarini et al. 2026). We plan to explore this in detail in a subsequent paper.

ACKNOWLEDGEMENTS

We thank Jim Fuller for his insights on tidally perturbed pulsators. AM and JS gratefully acknowledge support from the Science and Technology Facilities Council (STFC) under grant number ST/Y002563/1. DMB gratefully acknowledges UK Research and Innovation (UKRI) in the form of a Frontier Research grant under the UK government's ERC Horizon Europe funding guarantee (SYMPHONY; PI Bowman; grant number: EP/Y031059/1), and a Royal Society University Research Fellowship (PI Bowman; grant number: URF\R1\231631). SR is supported by the Swiss National Funding under project No. 212143. SR is a Postdoctoral Researcher of the Fonds de la Recherche Scientifique (FNRS) and supported by the L'Oréal-UNESCO For Women In Sciences Programme. GH's contribution to this research was supported in part by the Polish National Center for Science (NCN) through grant 2021/43/B/ST9/02972.

This work is based on observations made with the Mercator Telescope, operated on the island of La Palma by the Flemish Community, at the Spanish Observatorio del Roque de los Muchachos of the Instituto de Astrofísica de Canarias. Mercator operates through the IRI-FWO project (I000521N). The observations are obtained with the HERMES spectrograph, which is supported by the Research Foundation of Flanders (FWO), Belgium, the Research Council of KU Leuven, Belgium, the Fonds National de la Recherche Scientifique (FNRS), Belgium, the Royal Observatory of Belgium, the Observatoire de Geneva, Switzerland, and the Thüringer Landessternwarte Tautenburg, Germany. This paper includes data collected by the *TESS* mission, which are publicly available from the Mikulski Archive for Space Telescopes (MAST). Funding for the *TESS* mission is provided by NASA's Science Mission Directorate. This work used the TOPCAT software (Taylor 2005), the SIMBAD database (Wenger et al. 2000), and the Astrophysics Data System, funded by NASA under Cooperative Agreement 80NSSC25M7105. The PHOEBE2 modelling used the greenHPC facility at Keele University, which is supported by the Wolfson Foundation's Funding for places grant. This work used Microsoft Copilot to convert equations in the text to code and to survey the literature. No AI tools have been used to produce any text in this manuscript.

DATA AVAILABILITY

The *TESS* data used in this work are publicly available via the MAST website: `https://archive.stsci.edu/missions-and-data/tess`. The HERMES spectra used in this work are publicly available at `https://www.mercator.iac.es/instruments/hermes/archive/`. The times of eclipse minima and the variable frequency solution can be found in the online version of the manuscript.

REFERENCES

Abt H. A., Guzik J. A., Jackiewicz J., 2023, PASP, 135, 124201
Aerts C., Christensen-Dalsgaard J., Kurtz D. W., 2010, Asteroseismology, doi:10.1007/978-1-4020-5803-5.
Albrecht S., Reffert S., Snellen I. A. G., Winn J. N., 2009, Nature, 461, 373
Albrecht S., et al., 2014, ApJ, 785, 83
Aller A., Lillo-Box J., Jones D., Miranda L. F., Barceló Forteza S., 2020, A&A, 635, A128
Asplund M., Grevesse N., Sauval A. J., Scott P., 2009, ARA&A, 47, 481
Balona L. A., 2018, MNRAS, 476, 4840
Baran A. S., Koen C., 2021, Acta Astron., 71, 113
Barker A. J., 2022, ApJ, 927, L36
Baum A. C., Pepper J., Davenport J. R. A., Howell S. B., 2025, AJ, 170, 331
Bigot L., Dziembowski W. A., 2002, A&A, 391, 235
Bíró I. B., Nuspl J., 2011, MNRAS, 416, 1601
Bowman D. M., 2017, Amplitude Modulation of Pulsation Modes in Delta Scuti Stars, doi:10.1007/978-3-319-66649-5.
Bowman D. M., 2020, Frontiers in Astronomy and Space Sciences, 7, 70
Bowman D. M., Kurtz D. W., Breger M., Murphy S. J., Holdsworth D. L., 2016, MNRAS, 460, 1970
Bowman D. M., Johnston C., Tkachenko A., Mkrtichian D. E., Gunsriwiwat K., Aerts C., 2019, ApJ, 883, L26
Bowman D. M., Hermans J., Daszyńska-Daszkiewicz J., Holdsworth D. L., Tkachenko A., Murphy S. J., Smalley B., Kurtz D. W., 2021, MNRAS, 504, 4039
Breger M., 2000, MNRAS, 313, 129
Breger M., Montgomery M. H., 2014, ApJ, 783, 89
Burssens S., et al., 2023, Nature Astronomy, 7, 913
Carrell K., et al., 2024, ApJ, 973, 157

Choi J., Dotter A., Conroy C., Cantiello M., Paxton B., Johnson B. D., 2016, ApJ, 823, 102
Claret A., 2017, A&A, 600, A30
Conroy K. E., et al., 2020, ApJS, 250, 34
Degroote P., 2013, MNRAS, 431, 2554
Degroote P., et al., 2009, A&A, 506, 111
Dotter A., 2016, ApJS, 222, 8
Duguid C. D., Barker A. J., Jones C. A., 2020, MNRAS, 491, 923
Esseldeurs M., Mathis S., Decin L., 2024, A&A, 690, A266
Eze C. I., Handler G., 2024, The Astrophysical Journal Supplement Series, 272, 25
Fuller J., 2017, MNRAS, 472, 1538
Fuller J., 2021, MNRAS, 501, 483
Fuller J., Lai D., 2012a, MNRAS, 420, 3126
Fuller J., Lai D., 2012b, MNRAS, 421, 426
Fuller J., Hambleton K., Shporer A., Isaacson H., Thompson S., 2017, MNRAS, 472, L25
Fuller J., Kurtz D. W., Handler G., Rappaport S., 2020, MNRAS, 498, 5730
Fuller J., Rappaport S., Jayaraman R., Kurtz D., Handler G., 2025, ApJ, 979, 80
Gaia Collaboration et al., 2023, A&A, 674, A1
Giménez A., Bastero M., 1995, Ap&SS, 226, 99
Goodman J., Weare J., 2010, Communications in Applied Mathematics and Computational Science, 5, 65
Guo Z., 2021, Frontiers in Astronomy and Space Sciences, 8, 67
Hambleton K. M., et al., 2013, MNRAS, 434, 925
Handler G., WET network of collaborators 2013, in Krzesiński J., Stachowski G., Moskalik P., Bajan K., eds, Astronomical Society of the Pacific Conference Series Vol. 469, 18th European White Dwarf Workshop.. p. 53
Handler G., et al., 2020, Nature Astronomy, 4, 684
Handler G., Jayaraman R., Kurtz D. W., Fuller J., Rappaport S. A., 2022, in Szuszkiewicz E., et al., eds, Vol. 12, XL Polish Astronomical Society Meeting. pp 183–186 (`arXiv:2201.01722`), doi:10.48550/arXiv.2201.01722
Handler G., et al., 2025, A&A, 702, A104
Hejlesen P. M., 1987, A&AS, 69, 251
Henneco J., Bowman D. M., 2026, MNRAS, 549, stag1132
Henneco J., Schneider F. R. N., Heller M., Hekker S., Aerts C., 2025, A&A, 698, A49
Horvat M., Conroy K. E., Pablo H., Hambleton K. M., Kochoska A., Giammarco J., Prša A., 2018, ApJS, 237, 26
Hut P., 1981, A&A, 99, 126
Jayaraman R., Handler G., Rappaport S. A., Fuller J., Kurtz D. W., Charpinet S., Ricker G. R., 2022, ApJ, 928, L14
Jayaraman R., et al., 2024, ApJ, 975, 121
Jenkins J. M., et al., 2016, in Chiozzi G., Guzman J. C., eds, Society of Photo-Optical Instrumentation Engineers (SPIE) Conference Series Vol. 9913, Software and Cyberinfrastructure for Astronomy IV. p. 99133E, doi:10.1117/12.2233418
Jennings Z., Southworth J., Rappaport S. A., Borkovits T., Handler G., Kurtz D. W., 2024, MNRAS, 533, 2705
Jerzykiewicz M., et al., 2015, MNRAS, 454, 724
Johnston C., Tkachenko A., Van Reeth T., Bowman D. M., Pavlovski K., Sana H., Sekaran S., 2023, A&A, 670, A167
Jones D., et al., 2020, ApJS, 247, 63
Kahraman Aliçavuş F., et al., 2022, MNRAS, 510, 1413
Kepler S. O., et al., 2003, A&A, 401, 639
Kołaczek-Szymański P. A., Pigulski A., Michalska G., Moździerski D., Różański T., 2021, A&A, 647, A12
Kurtz D. W., 1982, MNRAS, 200, 807
Kurtz D. W., 2022, ARA&A, 60, 31
Kurtz D. W., et al., 2020, MNRAS, 494, 5118
Kurtz D. W., et al., 2025, MNRAS, 536, 2103
Kushnir D., Zaldarriaga M., Kollmeier J. A., Waldman R., 2017, MNRAS, 467, 2146
Laur J., et al., 2015, A&A, 581, A37
Lenz P., Breger M., 2005, Communications in Asteroseismology, 146, 53
Lightkurve Collaboration et al., 2018, Lightkurve: Kepler and TESS time series analysis in Python, Astrophysics Source Code Library (ascl:1812.013)
Marcadon F., Prša A., 2024, ApJ, 976, 242
Markova N., Cantiello M., Grassitelli L., 2025, A&A, 701, A297
McLaughlin D. B., 1924, ApJ, 60, 22
Medupe R., Kurtz D. W., Elkin V. G., Mguda Z., Mathys G., 2015, MNRAS, 446, 1347
Michielsen M., Pedersen M. G., Augustson K. C., Mathis S., Aerts C., 2019, A&A, 628, A76
Miszuda A., Guo Z., Townsend R. H. D., 2025, A&A, 702, A203
Moharana A., et al., 2026, MNRAS, 548, stag772
Murphy S. J., Grigahcène A., Niemczura E., Kurtz D. W., Uytterhoeven K., 2012, MNRAS, 427, 1418
Napier W. M., 1968, Ap&SS, 2, 61
Nelder J. A., Mead R., 1965, The Computer Journal, 7, 308
Newville M., et al., 2025, LMFIT: Non-Linear Least-Squares Minimization and Curve-Fitting for Python, doi:10.5281/zenodo.16175987, `https://doi.org/10.5281/zenodo.16175987`
Offner S. S. R., Moe M., Kratter K. M., Sadavoy S. I., Jensen E. L. N., Tobin J. J., 2023, in Inutsuka S., Aikawa Y., Muto T., Tomida K., Tamura M., eds, Astronomical Society of the Pacific Conference Series Vol. 534, Protostars and Planets VII. p. 275 (`arXiv:2203.10066`), doi:10.48550/arXiv.2203.10066
Ogilvie G. I., Lesur G., 2012, MNRAS, 422, 1975
Pavlovski K., Southworth J., 2009, MNRAS, 394, 1519
Pavlovski K., Southworth J., Tamajo E., 2018, MNRAS, 481, 3129
Prša A., et al., 2016, ApJS, 227, 29
Randich S., et al., 2022, A&A, 666, A121
Rappaport S. A., et al., 2021, MNRAS, 503, 254
Raskin G., et al., 2011, A&A, 526, A69
Ricker G. R., et al., 2015, Journal of Astronomical Telescopes, Instruments, and Systems, 1, 014003
Rossiter R. A., 1924, ApJ, 60, 15
Rosu S., Rauw G., Farnir M., Dupret M.-A., Noels A., 2022a, A&A, 660, A120
Rosu S., Rauw G., Nazé Y., Gosset E., Sterken C., 2022b, A&A, 664, A98
Rosu S., Sciarini L., Ekström S., Eggenberger P., Josiek J., Hirschi R., Georgy C., 2026, A&A, 712, A42
Rucinski S. M., 1992, AJ, 104, 1968
Rucinski S., 1999, in Hearnshaw J. B., Scarfe C. D., eds, Astronomical Society of the Pacific Conference Series Vol. 185, IAU Colloq. 170: Precise Stellar Radial Velocities. p. 82 (`arXiv:astro-ph/9807327`), doi:10.48550/arXiv.astro-ph/9807327
Rui N. Z., Fuller J., 2021, MNRAS, 508, 1618
Sana H., et al., 2012, Science, 337, 444
Sana H., et al., 2013, A&A, 550, A107
Savonije G. J., Papaloizou J. C. B., 1984, MNRAS, 207, 685
Sciarini L., Ekström S., Eggenberger P., Meynet G., Fragos T., Song H. F., 2024, A&A, 681, L1
Sciarini L., Rosu S., Ekström S., Marchand M., Eggenberger P., Meynet G., 2026, A&A, 707, A22
Serebriakova N., Tkachenko A., Johnston C., Pavlovski K., Aerts C., 2025, A&A, 699, A304
Shibahashi H., Aerts C., 2000, ApJ, 531, L143
Sirotkin F. V., Kim W.-T., 2009, ApJ, 698, 715
Southworth J., 2013, A&A, 557, A119
Southworth J., 2026, arXiv e-prints, p. arXiv:2606.04870
Southworth J., Bowman D. M., 2022, MNRAS, 513, 3191
Southworth J., Bowman D. M., 2026, ARA&A, 64, 223
Southworth J., Maxted P. F. L., Smalley B., 2004, MNRAS, 351, 1277
Southworth J., Bowman D. M., Tkachenko A., Pavlovski K., 2020, MNRAS, 497, L19
Southworth J., Bowman D. M., Pavlovski K., 2021, MNRAS, 501, L65
Steindl T., Zwintz K., Bowman D. M., 2021, A&A, 645, A119
Taylor M. B., 2005, in Shopbell P., Britton M., Ebert R., eds, Astronomical Society of the Pacific Conference Series Vol. 347, Astronomical Data Analysis Software and Systems XIV. p. 29
Tkachenko A., et al., 2016, MNRAS, 458, 1964

Tkachenko A., Pavlovski K., Serebriakova N., Bowman D. M., IJspeert L., Gebruers S., Southworth J., 2024, A&A, 683, A252
Turner D. G., Savoy J., Derrah J., Abdel-Sabour Abdel-Latif M., Berdnikov L. N., 2005, PASP, 117, 207
Van Reeth T., Southworth J., Van Beeck J., Bowman D. M., 2022, A&A, 659, A177
Van Reeth T., Johnston C., Southworth J., Fuller J., Bowman D. M., Poniatowski L., Van Beeck J., 2023, A&A, 671, A121
Vanlaer V., Bowman D. M., Burssens S., Bharati Das S., Bugnet L., Mathis S., Aerts C., 2025, A&A, 701, A5
Wachmann A. A., 1973, A&A, 25, 157
Wagg T., Johnston C., Bellinger E. P., Renzo M., Townsend R., de Mink S. E., 2024, A&A, 687, A222
Wenger M., et al., 2000, A&AS, 143, 9
Wolberg J., 2006, Data Analysis Using the Method of Least Squares: Extracting the Most Information from Experiments. Springer Berlin Heidelberg, https://books.google.co.in/books?id=BYYe-AYas9AC
Zahn J. P., 1975, A&A, 41, 329
Zahn J. P., 1977, A&A, 57, 383
Zahn J.-P., Bouchet L., 1989, A&A, 223, 112
Zhang V., Rappaport S., Jayaraman R., Kurtz D. W., Handler G., Fuller J., Borkovits T., 2024, MNRAS, 528, 3378
Zong W., Charpinet S., Vauclair G., Giammichele N., Van Grootel V., 2016a, A&A, 585, A22
Zong W., Charpinet S., Vauclair G., 2016b, A&A, 594, A46

APPENDIX A: EXTRACTED LIGHT CURVES

The *TESS* light curves and their corresponding pulsation light curves are shown in Fig. A1.

APPENDIX B: RV TABLES

The extracted RVs are given in Table B1. We also report the primary star's RVs after removing the pulsation signature, as explained in section 2.2.

APPENDIX C: PHOEBE2 JOINT SOLUTIONS VERSUS LIGHT CURVE SOLUTIONS

The final joint, light curve, and RV solution was accepted from the MCMC chains after estimating a burn-in and convergence by using the autocorrelation function (ACF; Goodman & Weare 2010). The final MCMC-sampled parameters, from the joint solution, are given in Table C1 and their correlations are shown in Fig. C1.

We also compared the joint solution with light curve only solutions from different sector segments. We sampled these light curves individually with 800 points in the eclipse phase and 200 in the out-of-eclipse phase. We fixed the parameters that are dependent on RV and apsidal analysis (e.g., e, M_1, M_2, $\dot{\omega}$). We optimised the parameters $r_1 + r_2$, k, i, $T_{\rm ratio}$, ω, $L_{\rm pb,1}$ and l_3 using the Nelder-Mead algorithm. Each sector was optimised for 200 iterations. We then sampled around the final Nelder-Mead solution using MCMC for 1200 iterations with 30 walkers. We found that the solutions converged quicker than the joint solution and therefore used a burn-in of 800 chains. The final MCMC correlations of the light curve solutions are given in Fig. C2 along with the MCMC correlations of the joint solution in grey.

APPENDIX D: TIDALLY PERTURBED PULSATORS IN THE LITERATURE

The list of TPPs in the literature with measurements of masses and radii is provided in Table D1. The Roche limit and orbital periods are also given.

APPENDIX E: FIXED FREQUENCY SOLUTIONS

We calculated a fixed-frequency solution to rule out any degeneracy between frequency variation, amplitude, and phase variation observed in the system.

We calculated the fixed-frequency solution for each sector segment. Like the free-frequency solution, we used the frequency solution for segment 81-82 as the trial solution for all other sector segments. But unlike the free-frequency solution, we fit only amplitudes and phases for sector segments 14-15, 54-55, and 74-75. These fits provided the solutions for the frequencies common to all sector segments. Then, to get the total solution for each sector segment, we extracted additional frequencies until the respective S/N limit was reached. The errors were calculated using the MCMC algorithm. The solutions are presented in Table E1. We found that amplitude variations were consistent in both our free-frequency and fixed-frequency solutions.

This paper has been typeset from a TEX/LATEX file prepared by the author.

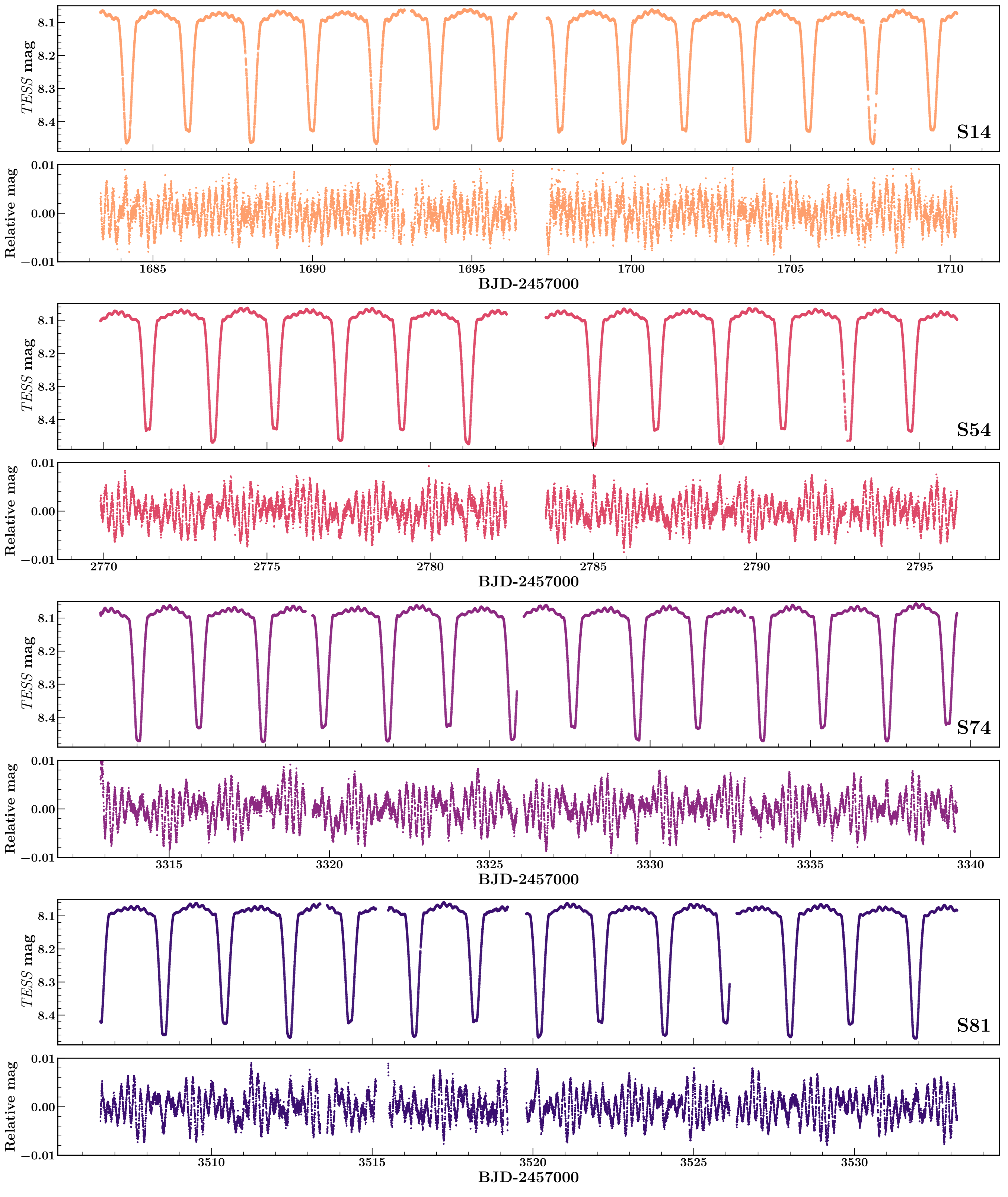

Figure A1. *TESS* light curves for different sectors and their corresponding extracted pulsation light curves.

Table B1. RVs extracted from HERMES spectroscopy. RV_1 corr. represents the RVs obtained after subtracting the pulsation signature and used for final binary modelling.

TBJD	RV_1 (km s^{-1})	RV_1 corr. (km s^{-1})	RV_1 Err.	RV_2 (km s^{-1})	RV_2 Err.
2418.434644	152.75	153.99	1.32	-239.66	3.63
2418.666598	133.08	139.23	1.49	-217.07	3.7
2419.642218	-80.95	-80.68	1.62	100.17	4.23
2420.443945	-188.12	-189.02	1.12	201.38	3.28
2420.657304	-169.5	-168.5	1.14	169.37	3.06
2421.641908	83.48	80.61	1.3	-113.65	5.08
2422.457841	147.87	145.82	1.09	-233.59	3.75
2422.665869	120.02	118.81	1.33	-201.39	3.36
2423.663774	-122.7	-125.57	0.93	121.19	2.64
2424.388596	-190.23	-185.69	0.94	194.23	3.14
2425.589169	80.55	86.88	0.83	-170.93	2.02
2426.429092	136.95	138.22	0.84	-218.52	2.72
2426.645355	107.27	106.16	0.86	-182.2	2.93
2427.523169	-115.32	-115.78	1.08	113.84	2.52
2427.643760	-149.46	-148.47	0.73	141.19	2.09
2428.381678	-181.81	-174.61	1.06	184.8	3.27
2430.430024	117.58	125.0	1.25	-200.84	3.56
2430.540822	106.58	103.99	1.06	-186.42	2.9
2430.689506	74.84	73.67	1.01	-142.56	3.77
2431.380604	-109.04	-106.7	1.18	107.33	2.93

Table C1. PHOEBE2 MCMC solution. More details about the PHOEBE2 parameters are available at: https://phoebe-project.org/docs/2.4/physics.

Parameter	PHOEBE2 parameter	Value
i [deg]	`inc@binary`	$87.27^{+0.28}_{-0.25}$
ω [deg]	`per0@binary`	$158.67^{+0.61}_{-0.59}$
k [deg]	`requivratio@binary`	$0.6273^{+0.0041}_{-0.0044}$
$r_1 + r_2$ [deg]	`requivsumfrac@binary`	$0.45446^{+0.00071}_{-0.00064}$
$L_{\rm pb,1}$ [W]	`pblum@primary`	$8.9^{+0.12}_{-0.11}$
l_3 [W m^{-2}]	`l3@dataset@lc01`	$0.0465^{+0.0091}_{-0.0085}$
M_1 [$M_\odot$]	`mass@primary`	$14.56^{+0.13}_{-0.13}$
M_2 [$M_\odot$]	`mass@binary`	$11.103^{+0.063}_{-0.065}$
$T_{\rm ratio}$	`teffratio@binary`	$0.96978^{+0.00086}_{-0.00084}$
v_γ [km s^{-1}]	`vgamma@system`	$-17.35^{+0.22}_{-0.22}$

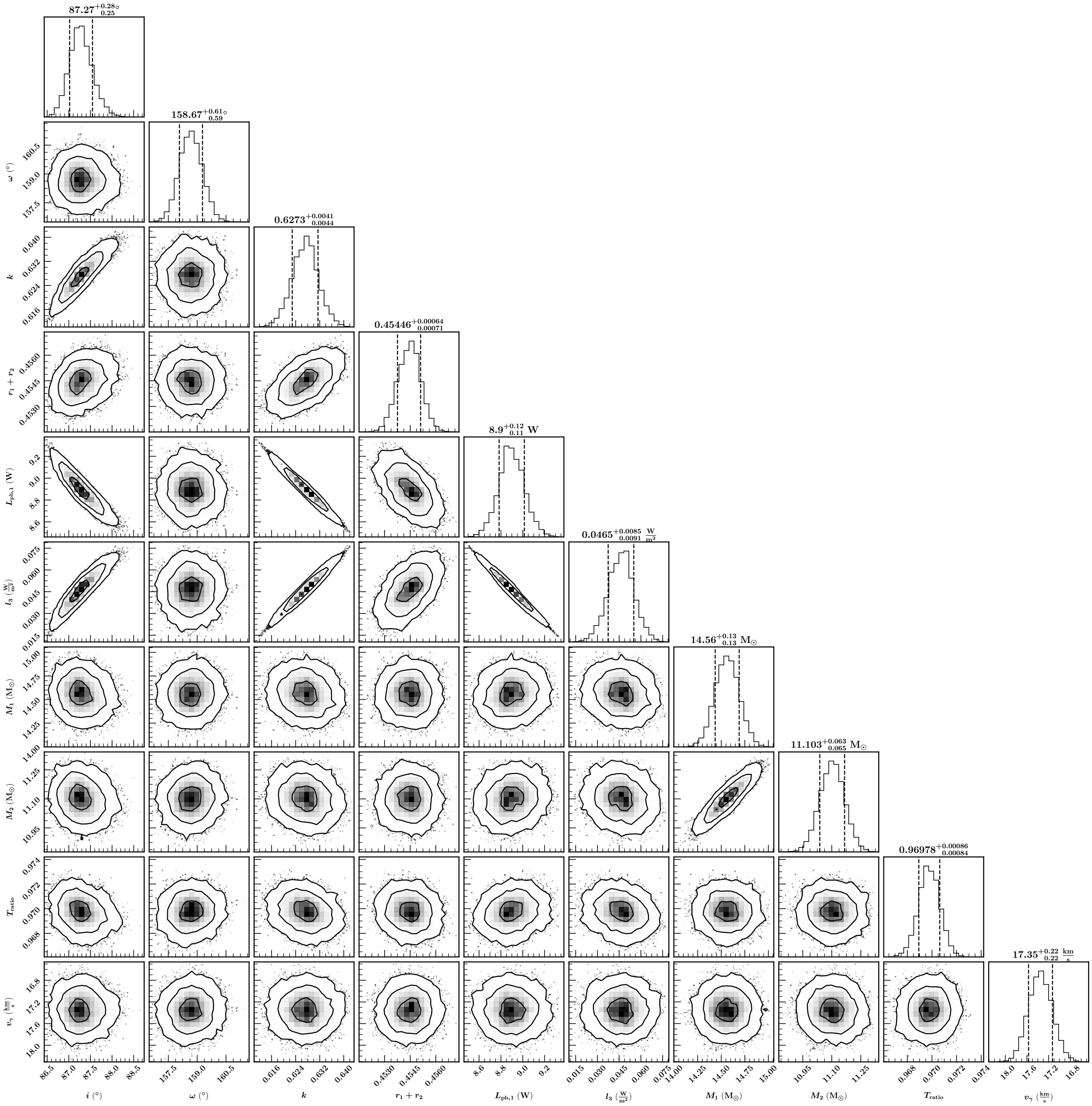

Figure C1. Corner plots for the PHOEBE2 MCMC sampling of stellar and orbital parameters using a joint RV and light curve (sector 41) model for V453 Cyg with constraints from apsidal motion analysis.

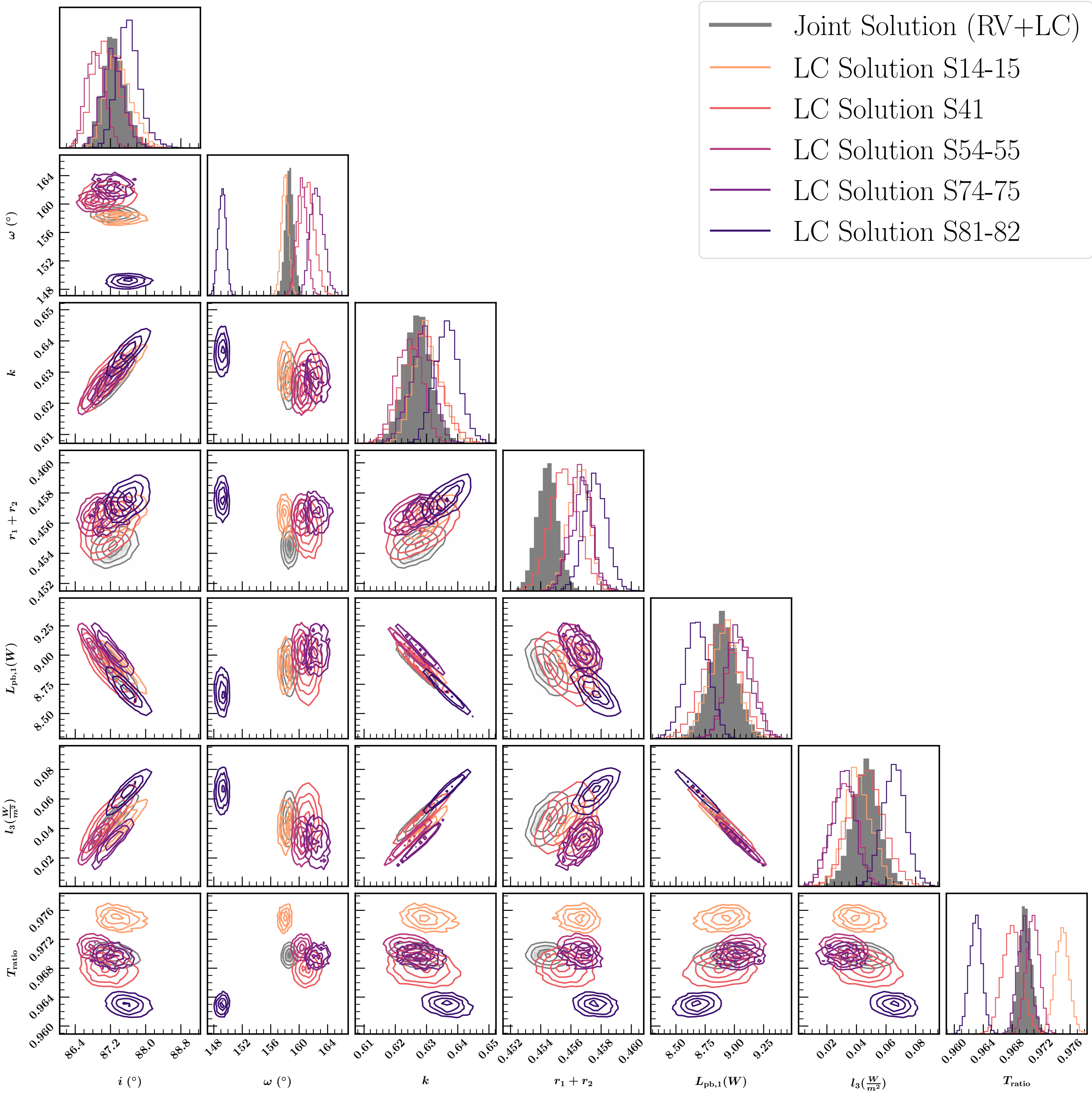

Figure C2. Corner plots for the PHOEBE2 MCMC sampling of stellar and orbital parameters using only *TESS* light curves. The filled grey histograms represent the MCMC distributions of the parameters obtained from the joint modelling.

Table D1. TPP in the literature.

System	$R/R_{\rm Roche}$		Period (d)	Source
	Pri.	Sec.		
TIC 63328020	0.98^{p}	0.99	1.1057	Rappaport et al. (2021)
CO Cam	0.73^{p}	0.74	1.2710	Kurtz et al. (2020)
KIC 4851217	0.48	0.64^{p}	2.4704	Jennings et al. (2024)
TIC 435850195	0.66^{p}	0.30	1.3672	Jayaraman et al. (2024)
TIC 184743498	0.66^{p}	0.59	1.0532	Zhang et al. (2024)
HD 265435	0.82^{p}	3.01	0.0688	Jayaraman et al. (2022)
RS Cha	0.62	0.69^{p}	1.6699	Steindl et al. (2021)
TZ Dra	0.65^{p}	0.99	0.8660	Kahraman Aliçavuş et al. (2022)
EL CMi	0.71^{p}	0.99	1.0538	Handler et al. (2025)[1]
VV Ori	0.83^{p}	0.60	1.4854	Southworth et al. (2021)
U Gru	0.59^{p}	0.96	1.8805	Johnston et al. (2023)
KIC 3228863	0.87^{p}	0.99	0.7309	Van Reeth et al. (2023)
V456 Cyg	0.68	0.70^{p}	0.8912	Van Reeth et al. (2022)

^{p} identified perturbed component. [1] from PHOEBE2 solution.

Table E1. Fixed frequency solution for different datasets.

				Sectors 14-15		Sectors 54-55		Sectors 74-75		Sectors 81-82	
No.	f (d^{-1})	N	f-N$\times f_{\rm orb}$	A (mmag)	ϕ (rad)	A (mmag)	ϕ (rad)	A (mmag)	ϕ (rad)	A (mmag)	ϕ (rad)
f_1	0.7710(3)	2	0.2569(3)	0.60(4)	0.9(3)	0.63(2)	0.136(4)	0.62(1)	0.267(3)	0.54(2)	0.301(6)
f_2	1.0288(2)	4	0.0005(2)	0.86(2)	0.263(4)	0.42(2)	0.502(6)	0.87(1)	0.123(2)	0.79(2)	0.007(4)
f_3	1.5452(5)	6	0.0027(5)	0.76(2)	0.321(4)	0.49(2)	0.246(5)	0.467(9)	0.633(3)	0.41(2)	0.005(7)
f_4	2.1168(6)	8	0.0601(6)	0.35(2)	0.04(1)	0.29(2)	0.524(9)	0.264(9)	0.346(7)	0.32(2)	0.59(1)
f_5	2.3746(6)	9	0.0609(6)	0.37(3)	0.52(1)	0.36(2)	0.256(7)	0.44(1)	0.632(3)	0.38(2)	0.743(9)
f_6	2.6298(6)	10	0.0590(6)	0.20(2)	0.27(2)	-	-	-	-	0.34(2)	0.794(9)
f_7	2.8906(6)	11	0.0627(6)	0.41(2)	0.877(9)	0.38(2)	0.588(7)	0.27(1)	0.939(5)	0.33(2)	0.65(1)
f_8	3.1510(7)	12	0.0660(7)	0.31(2)	0.29(1)	0.37(2)	0.401(8)	-	-	0.28(2)	0.03(2)
f_9	3.428(2)	13	0.086(2)	-	-	0.26(2)	0.41(1)	-	-	0.3(2)	0.7(6)
f_{10}	3.9203(5)	15	0.0641(5)	-	-	0.25(2)	0.234(8)	0.50(1)	0.722(2)	0.40(2)	0.116(8)
f_{11}	4.4316(2)	17	0.0612(2)	0.88(2)	0.259(4)	1.12(2)	0.672(3)	1.15(1)	0.882(1)	1.11(2)	0.941(3)
f_{12}	4.94592(8)	19	0.06137(8)	3.11(2)	0.912(1)	2.72(2)	0.100(1)	2.87(1)	0.1940(6)	2.81(2)	0.223(1)
f_{13}	5.4601(2)	21	0.0614(2)	-	-	0.54(2)	0.670(6)	0.818(9)	0.742(2)	0.74(2)	0.721(5)
f_{14}	5.9754(4)	23	0.0625(4)	-	-	-	-	0.426(9)	0.247(4)	0.39(2)	0.014(6)
f_{15}	7.517(2)	29	0.062(2)	0.1(1)	0.4(4)	-	-	-	-	0.09(2)	0.63(4)
f_{16}	8.029(2)	31	0.060(2)	0.10(9)	0.8(5)	-	-	-	-	0.09(2)	0.44(3)
f_{17}	9.876(1)	38	0.107(1)	0.16(2)	0.48(2)	0.18(4)	0.4(1)	0.19(1)	0.903(7)	0.18(2)	0.73(2)
f_{18}	10.5073(8)	40	0.2241(8)	0.27(7)	0.59(2)	0.2(2)	0.2(7)	0.23(3)	0.02(1)	0.24(2)	0.93(1)
f_{19}	11.708(3)	45	0.139(3)	-	-	0.09(8)	0.6(4)	0.09(4)	0.1(2)	0.04(2)	0.66(3)
f_{20}	19.53(2)	75	0.24(2)	0.02(3)	0.8(4)	-	-	-	-	0.03(2)	0.8(1)
f_{21}	19.80(2)	77	-	-	-	0.02(2)	0.4(4)	0.02(1)	0.5(2)	-	-
f_{22}	28.26(2)	109	0.24(2)	-	-	-	-	0.01(1)	0.1(2)	0.01(2)	0.9(7)
f_{23}	32.37(2)	125	0.24(2)	0.02(2)	0.6(6)	-	-	0.005(8)	0.4(3)	-	-
f_{24}	43.85(2)	170	0.15(2)	0.01(2)	0.8(5)	-	-	0.001(7)	0.4(3)	-	-